TOWARD CHARACTERIZATION OF DISEASED VASCULAR STRUCTURES USING NONCONTACT PHOTOACOUSTIC AND LASER-ULTRASOUND IMAGING: A PHANTOM STUDY

by

Jami Lynne Johnson

A thesis

submitted in partial fulfillment

of the requirements for the degree of

Master of Science in Mechanical Engineering

Boise State University

May 2013

BOISE STATE UNIVERSITY GRADUATE COLLEGE

DEFENSE COMMITTEE AND FINAL READING APPROVALS

of the thesis submitted by

Jami Lynne Johnson

Thesis Title: Toward characterization of diseased vascular structures using noncontact photoacoustic and laser-ultrasound imaging: a phantom study

Date of Final Oral Examination: 07 March 2013

The following individuals read and discussed the thesis submitted by student Jami Lynne Johnson, and they evaluated her presentation and response to questions during the final oral examination. They found that the student passed the final oral examination.

Michelle Sabick, Ph.D.   Chair, Supervisory Committee

Kasper van Wijk, Ph.D.   Member, Supervisory Committee

Trevor Lujan, Ph.D.   Member, Supervisory Committee

The final reading approval of the thesis was granted by Michelle Sabick, Ph.D., Chair of the Supervisory Committee. The thesis was approved for the Graduate College by John R. Pelton, Ph.D., Dean of the Graduate College.

For Amanda Joy, whose courage and true joy at only 10 years of age are inspiring.

ACKNOWLEDGMENT

I would like to take this opportunity to thank several people for their support throughout my time at Boise State University. First, I would like to thank my advisor and committee chair, Dr. Michelle Sabick, for all of her support over the past two years. I have had the opportunity to gain experience in a wide spectrum of research, academics, and interdisciplinary collaborations thanks to the doors she has opened. My excitement for research, academia, and innovation has significantly grown since I began my work under her guidance at BSU.

I would also like to thank the members of my thesis committee. I must thank Dr. Kasper Van Wijk for his excitement in entering a new research application. I am thankful for both the use of his laboratory and equipment, as well as his guidance in the experimental, technical, and academic aspects required for this thesis. I would like to thank Dr. Trevor Lujan for his service and the beneficial research and writing tools he passed on to me. His expertise was much appreciated, and I believe the skills I learned will equip me well for future work.

I would also like to thank Dr. Thomas Blum for teaching me the "ins-and-outs" of the Physical Acoustics Lab, and for guiding my work and understanding from the start of this thesis.

I would like to thank my undergraduate advisor, Dr. Chad Hoyt. The introduction to molecular optics, research experience, and problem-solving skills I learned as an undergraduate have been an invaluable asset for my work as a master's student.

I gratefully acknowledge the Office of University and Industry Ventures and the Innovation Team for their support during my time at Boise State. I appreciate the

skills regarding needs-based development and the insight into commercialization and industry I obtained. I am exceptionally thankful for the joint graduate assistantship from the Office of University and Industry Ventures and the Mechanical and Biomedical Engineering department that supported me for the past two years. My graduate studies would not have been possible without it.

I would like to express my deep thanks to my family. They have provided the utmost support and encouragement to me as a graduate student, and in all of my endeavors.

ABSTRACT

Visualizing and characterizing atherosclerotic plaques is important in determining the vulnerability of a plaque to rupture. To evaluate rupture risk, several compositional factors should be evaluated, including inflammation, the presence and size of lipid pools, thickness of the fibrous cap, and calcification. Currently, a need exists for an imaging modality that can detect each of these factors in a safe, noninvasive manner with high resolution and contrast at clinically relevant depths. Photoacoustic imaging is a growing field that has the potential to improve plaque diagnosis. Spectroscopic methods have shown promise toward detection of constituents of plaque with unique optical absorption spectra, such as lipids; however, detection of molecules with indistinct spectra, such as calcium, is not readily achieved using this approach. The acoustic properties of calcium, in contrast, are different than soft tissue, which causes calcification to scatter acoustic waves.

In this work, a method of evaluating both spectroscopic and acoustic properties of vascular structures is presented by combining photoacoustic (PA) and laser-ultrasound (LU) techniques. These methods could inform treatment decisions and improve patient outcomes by detecting the smallest plaque and calcification deposits in the early stages of disease. When the disease has progressed to a later stage, such that surgical intervention is required, PA and LU imaging could inform surgical decisions to ensure that appropriate precautions are taken and the least-risk procedure is chosen.

Experiments on tissue phantoms were conducted with healthy and diseased artery surrogates embedded. All imaging was accomplished using noncontact, noninvasive

PA and LU imaging. Through implementation of geophysical image processing techniques, improved image resolution and a method of comparing contrast among optical absorbers and acoustic scatterers was demonstrated. Absorbing structures on the order of 1.5 mm were clearly identified, and acoustic scattering by stiff structures with a wall thickness of 233.5 μm was detected at a depth of 18 mm. The results demonstrate that dual photoacoustic and laser-ultrasound imaging has the potential to characterize multiple constituents of atherosclerotic plaque in a safe, noninvasive manner.

TABLE OF CONTENTS

ix

LIST OF TABLES

LIST OF FIGURES

CHAPTER 1:

THE PROBLEM OF ATHEROSCLEROSIS

The most common cause of death and disabilities globally is cardiovascular disease, accounting for around 17 million deaths each year (Mendis *et al.*, 2011). A majority of cardiovascular events, such as myocardial infarction and cerebrovascular events, are a result of atherosclerosis, a progressive disease of the blood vessels (Mendis *et al.*, 2011; Wang, 2009; Wexler *et al.*, 1996).

Atherosclerosis is characterized by a buildup of plaque on the inside surface of the arteries, which can cause vessels to become irregularly shaped, narrow, stiff, and difficult for blood to flow through. If these deposits rupture, thrombosis and occlusion may occur, leading to vascular events such as heart attack and stroke (Wexler *et al.*, 1996; Wang, 2009; Mendis *et al.*, 2011; Rhoades and Pflanzer, 2003). If a clot completely occludes the coronary artery, the heart muscle may die due to insufficient oxygenation (Richards-Kortum, 2010). If a plaque ruptures in the brain, a stroke may follow. It is suspected that plaque rupture is the cause of 60% or more of deaths in patients with sudden coronary death and thrombosis (Burke *et al.*, 1997; Naghavi *et al.*, 2003). Diseases of the aorta and arteries, including hypertension and peripheral vascular disease, are also often due to atherosclerosis (Mendis *et al.*, 2011). Substantial disability can result from peripheral vascular diseases, and the severity of the disease is closely associated with increased risk of death from vascular causes (Alnaeb *et al.*, 2007).

The composition of plaque is important in identifying deposits that are vulnerable
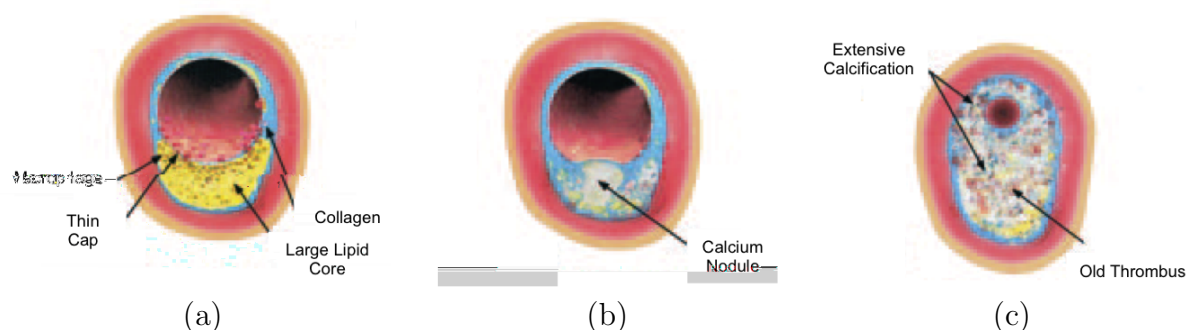
Figure 1.1: Three types of plaque that may cause cardiovascular events. (a) Plaque that is rupture-prone, with a large lipid core and thin fibrous cap, infiltrated by macrophages. (b) Plaque with calcified nodule protruding into the vessel lumen. (c) Chronically stenotic plaque with an eccentric lumen, old thrombus, and extensive calcification. (Naghavi *et al.* (2003); From Vulnerable Plaque to Vulnerable Patient: A Call for New Definitions and Risk Assessment Strategies: Part I. Circulation, 108, 1664-1672). Reproduced with permission.

to rupture and to making treatment and intervention decisions accordingly. Several criteria should be considered when making a diagnosis, including the presence and size of lipid pools, thickness of the fibrous cap (connective tissue covering the lipid core), inflammation, and calcification, Figure 1.1 (Virmani *et al.*, 2000; Sethuraman *et al.*, 2005). Each of these factors will be discussed in further depth below.

1.1   Molecular Composition Factors

Several molecular factors contribute to plaque vulnerability, such as active inflammation and the presence of a thin fibrous cap with a large necrotic core (Naghavi *et al.*, 2003). Vulnerable necrotic cores generally consist of lipids, dead cells, and calcification (Fok, 2012). Large lipid cores that account for >40% of a plaque's total volume with a cap thickness < 100 μm are believed to contribute to atherosclerotic

plaque vulnerability (Kolodgie *et al.*, 2001).

The extent of inflammation and presence of macrophages near plaque deposits has also been related to plaque vulnerability (Pasterkamp *et al.*, 1999). In the beginning stages of atherosclerosis and coronary artery disease, a large amount of immune cells stimulate inflammation, encouraging the growth of lesions (Hansson, 2005). Additionally, the overall geometry of the atherosclerotic vessel may contribute to an increased risk of plaque rupture (Pasterkamp *et al.*, 1999).

With early detection, cost-effective pharmaceutical interventions and lifestyle modifications can help prevent the formation of dangerous atherosclerotic plaque (Mendis *et al.*, 2011; Hiratzka *et al.*, 2007). At later stages, a surgical intervention is often required. In many cases, a catheter intervention such as balloon angioplasty is sufficient, however, when plaque vulnerability or narrowing reaches a more severe stage, bypass surgery may be required (Roger *et al.*, 2011).

1.2   Calcification

The extent of calcification is an important factor in diagnosing and assessing cardiovascular disease. Atherosclerotic calcification is thought to be an active, organized, and regulated process that is similar to bone formation (Wexler *et al.*, 1996). The precise relationship of calcification to plaque rupture is unknown, however, the impact on plaque rupture may vary depending on the extent of calcification. If extensive calcification is present, rupture might be less likely (Schuijf *et al.*, 2007), but in earlier stages, plaque vulnerability may be enhanced due to increased stress at the interface of calcified and non-calcified atherosclerotic sections (Wexler *et al.*, 1996; Richardson *et al.*, 1989). Atherosclerotic calcification generally begins in the second or third

decade of life (Wexler *et al.*, 1996). However, active vascular calcification in the coronary-arteries in pediatric and hemodialysis patients ranging from 19-39 years of age is increasing (Raggi and Bellasi, 2007).

In a study of patients who died from sudden coronary death, all hearts showed some calcification by age 50 in men and women. For men and women younger than 40 years old, 55% showed some calcification (Burke *et al.*, 2000). The presence of coronary artery calcification has been shown to be an excellent predictor of the presence of atherosclerotic plaque, yet the absence of calcification does not necessarily rule out the presence of atherosclerotic plaque. Severe lumen obstruction is also improbable when coronary artery calcification is not present (Sangiorgi *et al.*, 1998).

Calcification is an important variable to consider for many additional cardiovascular conditions. Certain biomaterials, such as polytetrafluorethylene, are known to encourage calcification when implanted in the body. When calcium deposits accumulate in surgically implanted grafts, a loss of flexibility can lead to mechanical failure and degradation (Hayabuchi *et al.*, 2007). Degeneration and leaflet tearing are also concerns for calcified bioprosthetic heart valves (Jorge-Herrero *et al.*, 2010). Regardless of the cause, aortic valve calcification may be an independent predictor of future cardiovascular events (Gondrie *et al.*, 2010). In addition, lesions with calcification are generally associated with a lower success rate and increased complications for stenting procedures (Moussa *et al.*, 1997), and calcification left untreated after procedures such as coronary bypass surgery can lead to irreversible damage from stenosis (Holmgren *et al.*, 2012).

If detected prior to surgery, precautionary measures can be taken to reduce the risk of complications due to calcification for catheter interventions. This may involve

rotational atherotomy to cut away a portion of the deposit (Moussa *et al.*, 1997) or opting for a different surgical treatment. Rotational atherotomy can also be used to increase blood flow in arteries with vulnerable, calcified plaque. In contrast to the response of components such as lipids to pharmaceutical therapies, patients with large amounts of calcification are less likely to undergo changes in the extent of plaque in response to established cardiovascular risk-targeting medical therapies (Nicholls *et al.*, 2007).

Hemodialysis patients and breast cancer patients also have increased risks from calcification. Mitral and aortic valve calcification has shown to increase the risk of mortality for hemodialysis patients (Raggi *et al.*, 2011). Adverse outcomes are also associated with a higher prevalence of calcification in hemodialysis patients than patients with normal kidney function (Raggi and Bellasi, 2007). A recent study of routine mammography screenings concluded that women with mammographic vascular calcifications are at significantly higher risk for peripheral vascular disease (Dale *et al.*, 2006). In addition, the presence of calcification in women with breast cancer has shown to be a predictor of subsequent breast cancer (Thomas *et al.*, 2002, 1993).

1.3   Current Plaque Imaging Techniques

Currently, no clinical imaging modality has the ability to provide a comprehensive characterization of vulnerable atherosclerotic plaques. Molecular, functional, and mechanical information are important for a complete understanding of an atherosclerotic lesion. Modalities such as computed tomography (CT), angiography, magnetic resonance imaging (MRI), ultrasonography, fluoroscopy, and optical coherence tomography (OCT) have capabilities to detect specific components of atherosclerotic

plaque, yet each has limitations to full plaque characterization and widespread use.

1.3.1 Molecular and Functional Imaging Modalities

Several imaging modalities can detect certain molecular and functional characteristics of vulnerable plaque described in Section 1.1. These include OCT, intravascular ultrasound (IVUS), angiography, elastography, MRI, and spectroscopic methods (Naghavi *et al.*, 2003). Coronary angiography is often used to image arteries and evaluate if there are blockages. X-ray absorbing contrast dyes are injected into the arteries, allowing for high-contrast videos of blood flow to be obtained (Richards-Kortum, 2010). While general structure and artery size can be visualized with high-contrast, characterization of atherosclerotic lesions is not clear, nor recommended with angiography (Baumgart *et al.*, 1997).

Magnetic resonance imaging is one of the most reliable imaging modalities for assessing the composition of plaques, with the ability to image at the cellular and molecular level (Briley-Saebo *et al.*, 2007; Grimm *et al.*, 2012). MRI measures the interaction between hydrogen atoms in tissue water and magnetic fields from 0.5-2 Tesla (Richards-Kortum, 2010). In particular, imaging of lipid cores and intraplaque hemorrhage may benefit from multi-contrast MRI imaging for large arteries (Briley-Saebo *et al.*, 2007). Submillimeter resolution, 3D images of the arterial wall, and high soft tissue contrast are obtainable with MRI, however high cost, low signal-to-noise ratio, and motion artifact limit the widespread use of MRI for plaque screening (Richards-Kortum, 2010; Briley-Saebo *et al.*, 2007; Saam *et al.*, 2007).

Vibrational spectroscopic methods, such as Fourier transform infrared spectroscopy (FTIR) and Raman spectroscopy, provide a large amount of information about tissue

morphology and composition (Lattermann *et al.*, 2013). Recently, cholesterol ester, cholesterol, tripalmitin (a triglyceride), and collagen were identified using Raman and FTIR imaging of an atherosclerotic rabbit artery ex vivo. While biochemical and molecular information can be accurately obtained using these techniques, depth penetration is a constraint, which limits these methods to intravascular applications (Lattermann *et al.*, 2013).

Invasive OCT methods can image plaque volumes with resolutions of 10-20 μm, however significant time must be allocated for manual image segmentation and quantification (Wang *et al.*, 2010). This drawback, along with the need to invasively enter the artery, limits the use of OCT for widespread atherosclerosis risk assessment and screening.

1.3.2   Calcification Imaging Modalities

Several imaging modalities have the potential to detect calcification, including fluoroscopy, several CT modalities, IVUS, MRI, coronary angiography, and echocardiography. Most commonly, however, CT and fluoroscopy methods are used to detect deposits initially, with invasive measures such as IVUS used to view and evaluate specific deposits before surgical intervention (Wexler *et al.*, 1996).

Qualitative information regarding vascular calcification is often obtained using plain radiograpahy or ultrasonography (Raggi and Bellasi, 2007). For genitourinary and mitral valve leaflet calcification detection, X-ray computed tomography is commonly used, with ultrasonography or echocardiography used as a secondary measure (Taki *et al.*, 2012). Noninvasive echocardiography, an ultrasound modality, is considered the gold standard for cardiac-valve morphology characterization (Raggi and

Bellasi, 2007).

Computed tomography involves scanning an area from multiple directions within the same plane to obtain X-ray transmission data (Webster, 1998). X-ray penetration is significantly attenuated by calcium, which causes "blooming" artifacts with reconstruction algorithms for CT images (Arbab-Zadeh *et al.*, 2012). Typically, CT images utilize a slice thickness of about 1 cm, with lateral spatial resolution nearing 0.25 mm (Richards-Kortum, 2010). Slice thicknesses of 3 - 6 mm and scan times of about 100 ms are typical of electron beam computed tomography (EBCT) images (O'Rourke *et al.*, 2000). EBCT may be the only modality that can quantify the volume of calcium, however, reproducibility is a concern unless the calcified area is greater than 2 mm (Wexler *et al.*, 1996). An example of EBCT images of calcifications are shown in Figure 1.2.

In the last decade, multidetector computed tomography (MDCT) imaging has improved significantly. A slice thickness of 0.75 mm is typically used for image reconstruction, improving plaque characterization using CT. For a 64-slice MDCT image used for coronary angiography, the effective radiation dose is 11-22 mSv, or about 3 to 4 times the average yearly effective dose of natural background radiation (Hoffmann *et al.*, 2006). The gold standard for evaluating the extent and advancement of vascular calcification are EBCT and MDCT modalities, yet high cost and significant radiation exposure limit CT imaging for calcification screening (Raggi and Bellasi, 2007).

For the detection of breast cancer calcifications, mammography and ultrasound are typically used. Mammography has the ability to detect calcifications as small as about 0.1 to 0.2 mm (Taki *et al.*, 2012). While imaging small structures is continuing
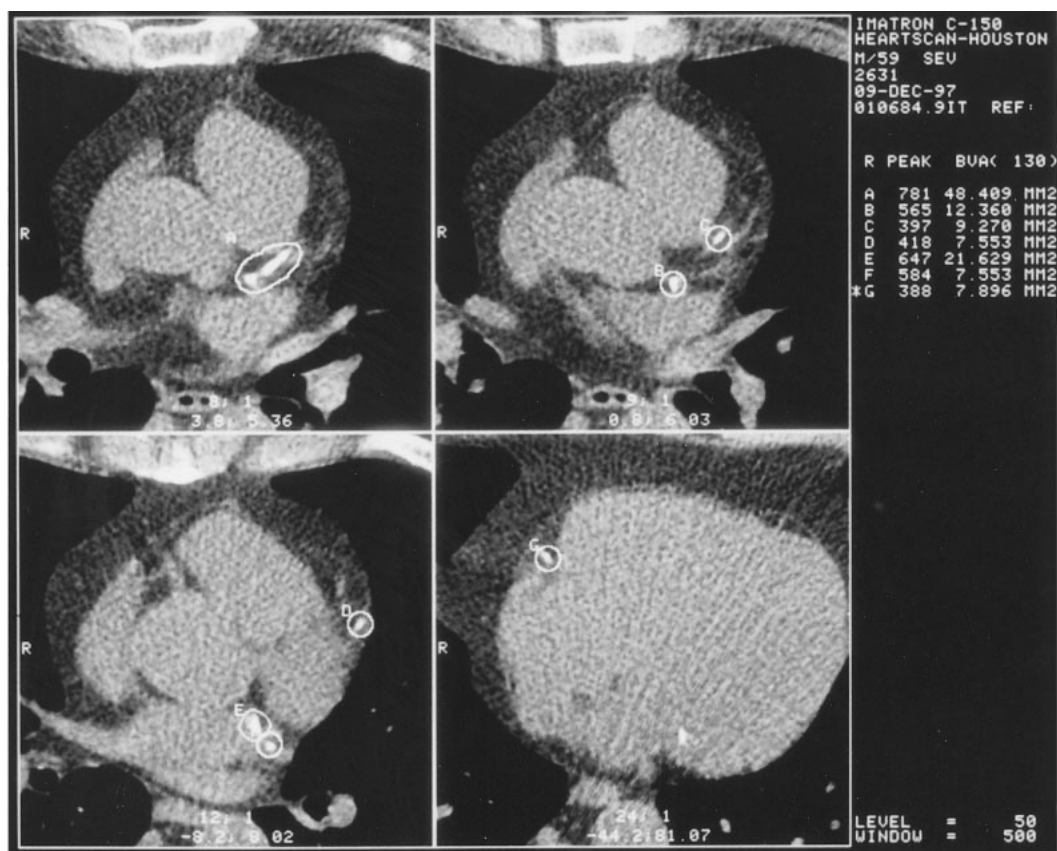
Figure 1.2: EBCT images of calcifications (circled) of multiple sizes. Corresponding deposit sizes are listed to the right of the images. Image used with permission (He *et al.*, 2000).

to improve with both CT and mammography, the use of ionizing X-ray radiation in these modalities is undesirable, and contributes additional health risks.

Fluoroscopy is used to acquire real-time images by placing the patient between an X-ray source and an image screen or monitor. This modality can accurately image medium to large calcific deposits, but smaller calcifications are unlikely to be detected. The availability and relative low cost of fluoroscopy are favorable, however disadvantages include the use of ionizing radiation, inability to quantify calcium, dependence on skill of the operator, and variability of equipment (Wexler *et al.*, 1996).

Ultrasound is a relatively low cost, portable, and safe imaging modality (Raggi and Bellasi, 2007). Calcification is typically distinguished in ultrasound images by a hyperechoic region, where the amplitude of the detected wave is increased, accompanied by acoustic shadowing, which occurs when the path of a sound wave is obstructed. Small calcifications, however, are seldom accompanied by acoustic shadowing because they exhibit low levels of blocking (Taki *et al.*, 2012). Ultrasound image slices are usually around 1 mm, with 0.5 mm in-plane lateral resolution (Richards-Kortum, 2010). In practice, traditional ultrasonography poorly predicts calcified lesions smaller than about 3 mm (Fowler *et al.*, 2002). An echocardiogram of a calcified mitral valve is shown in Figure 1.3.

Intravascular ultrasound imaging of the coronary arteries can obtain 0.05 - 0.1 mm resolution, however, higher frequencies are used that limit depth penetration to about 5 - 10 mm (Richards-Kortum, 2010). IVUS creates cross-sectional images using catheters with transducers mounted on the tip. An example of calcifications detected in atherosclerotic plaque with IVUS are shown in Figure 1.4. High sensitivity and
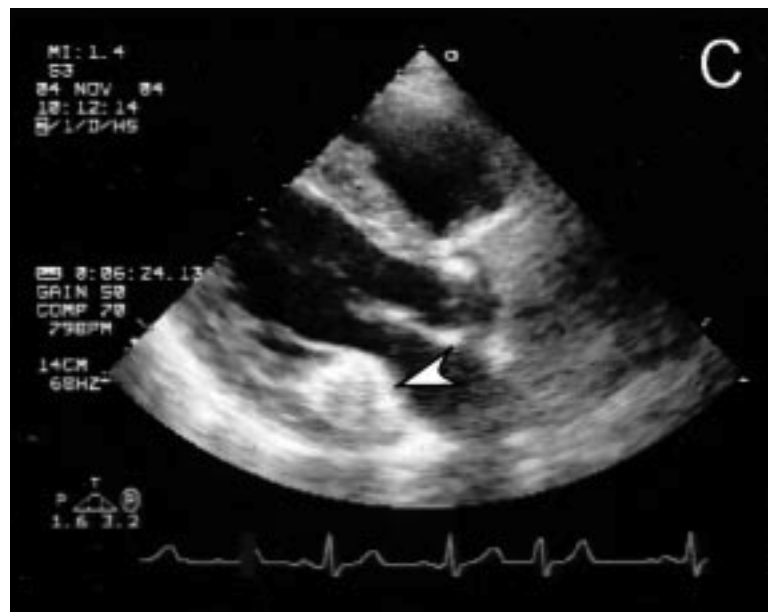
Figure 1.3: Echocardiogram of abnormal calcified mass on the mitral valve. Acoustic shadowing and hyperechoic behavior are evident. Image used with permission (Yokoyama *et al.*, 2007).
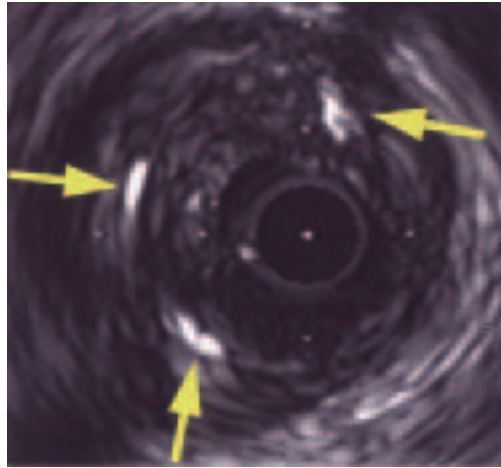
Figure 1.4: Cross-sectional images of calcifications in plaque detected with IVUS. Deposits are labeled with arrows. Image used with permission (Ehara *et al.*, 2004).

specificity for dense, coherent calcification have been reported (90% an 100%, respectively), where sensitivity drops significantly for areas of less than 0.05 mm^2 (64% reported) (Friedrich *et al.*, 1994; Wexler *et al.*, 1996). Hagenaars *et al.* (2000) found that measurements of the extent of calcification were highly reproducible for calcifications with an average (median) length of 88 mm. The invasive nature of intravascular imaging, cost, and additional operative time and equipment are obstacles that remain before implementation of IVUS for routine plaque characterization (Arthurs *et al.*, 2010). A summary of the modalities commonly used for plaque characterization is shown in Table 1.1.

Modality	Calcification	Deposit Resolution	Invasive	Ionizing	Molecular	Mechanical
MRI	limited	<1 mm	no	no	yes	no
Angiography	no	0.5 mm	yes	yes	no	no
Optical	no	20 μm	yes	no	yes	no
CT	yes	2 mm	no	yes	no	yes
Mammography	yes	$\approx$ 0.1 mm	no	yes	no	yes
Fluoroscopy	yes	$\approx$ 1 mm	no	yes	no	yes
Ultrasound	yes	3 mm	no	no	no	yes
Intravascular Ultrasound	yes	0.05 mm	yes	no	no	yes

Table 1.1: Summary of clinical imaging modalities used for characterization of atherosclerotic plaques.

1.3.3 Summary of Clinical Need

Plaque detection and characterization continues to improve with state-of-the-art imaging modalities. However, while several modalities provide exceptional resolution for particular constituents of atherosclerotic plaque, no modality can provide comprehensive characterization. Soft, molecular constituents such as lipid pools, in addition to stiff components like calcification, should be considered when determining the vulnerability of a plaque to rupture. Reliably imaging small calcifications, in particular, remains a challenge.

Overall, detecting the presence of atherosclerotic plaque and calcification early in the onset of disease can allow for preventative interventions to be made. At later stages, complete characterization of diseased vessels that require surgical intervention could inform surgical decisions and reduce the risk of complications.

Currently, no technique fully meets the diagnostic needs with sufficient resolution unless it is invasive and/or uses ionizing radiation. Therefore, there is a critical need to develop an imaging platform that can image molecular and mechanical information of plaque deposits with high resolution at clinically relevant depths in a

safe, noninvasive manner. In this work, we propose a method of exploiting both the optical (molecular) and acoustic (mechanical) properties of artery surrogates using noncontact photoacoustic and laser-ultrasound techniques. With this nonionizing, noninvasive method, we expect to detect structures on the order of 1 mm, and more importantly, detect changes in acoustic impedance for a wall thickness on the order of hundreds of micrometers at depths beyond 1 cm.

CHAPTER 2:

LASER-GENERATED ULTRASOUND IMAGING

Photoacoustic (PA) and laser-ultrasound (LU) imaging are rapidly expanding fields, which have most recently been applied to biomedical applications. Essentially, PA and LU imaging utilize laser-generated ultrasound, in which the absorption of light generates an acoustic wave.

Discovery of the photoacoustic effect dates back to 1880, when Alexander Graham Bell observed the absorption of modulated light resulting in audible sound (Bell, 1880). Strong promise for biomedical imaging applications, however, has only been apparent since the turn of the 21st century (Beard, 2011). Detection of laser-generated acoustic waves has also been explored for non-destructive material characterization (Li and Hayward, 2012), pharmaceutical tablet evaluation (Verghese and Cetinkaya, 2007; Akseli *et al.*, 2009), and geophysical applications (Blum *et al.*, 2011).

This chapter presents an overview of photoacoustic and laser-ultrasound imaging, and the application of these modalities to medical imaging. The basic theory of photoacoustic wave generation and ultrasound propagation is presented. In addition, advantages of PA and LU imaging are discussed, as well as the disadvantages and obstacles that have yet to be overcome.

2.1 Introduction to Photoacoustic Imaging

The photoacoustic (PA) effect begins with a modulated light source, typically a laser, incident on a partially transparent medium. Human tissue exhibits strong optical scattering properties, therefore the source light diffuses into a broad beam. A fraction of the laser energy penetrates up to centimeters into the tissue, approximately following the diffusion law (Xu and Wang, 2006). If the source wavelength corresponds to an absorption wavelength of a chromophore within the tissue, a portion of the pulse energy is absorbed by the chromophore and converted into heat. A subsequent increase in temperature, followed by an increase in pressure occurs. This rapid thermoelastic expansion results in emission of acoustic waves, which can be detected at the surface of the tissue. In brief, PA imaging is considered absorption based, where the transient pressure within the absorbing chromophore behaves as the initial source of ultrasound waves (Xu and Wang, 2006).

2.1.1 Advantages of Photoacoustic Imaging

Photoacoustic imaging possesses inherent advantages, which include the high contrast capabilities of spectroscopic imaging modalities and high resolution and multiple centimeter probing depths of ultrasound. Purely optical imaging modalities that rely on minimally scattered (ballistic) photons have high resolution capabilities, yet are limited to depths of about 1 mm. Modalities relying on multiscattered photons can reach multiple centimeters, at the cost of reduced resolution and blurring (Wang, 2009; Xu and Wang, 2006). Photoacoustic imaging, on the other hand, benefits from multiple optical scattering events, which allows for chromophores in tissue to be more evenly illuminated. Ultrasonic scattering is two to three orders of magnitude weaker than

optical scattering in tissue, therefore photoacoustic imaging allows for high spatial resolution deep within tissue (Yao and Wang, 2011; Wang, 2009). Furthermore, photoacoustic imaging utilizes low-intensity, nonionizing radiation. This eliminates the health hazards related to ionizing radiation, such as that used in X-ray or positron emission modalities (Wang, 2009).

Photoacoustic imaging is particularly well-suited for imaging vascular structures because the absorption coefficient of hemoglobin is significantly higher than surrounding tissues for wavelengths in the optical window, around 700-900 nm (Xu and Wang, 2006). As a result, the amplitude of the PA wave generated by hemoglobin molecules can be of high-contrast with the appropriate illumination wavelength. Because PA imaging is absorption based, spectroscopic information can be extracted. Oxygenation status, tumor characteristics, melanin concentration, and molecular imaging are all applications that may benefit from this modality (Wang, 2009).

2.1.2 Theory of the Photoacoustic Source

The spectroscopic capabilities of PA imaging are a clear advantage, yet a common misconception is that the amplitude of a PA wave can be directly related to absorption, when in fact the problem is more complex (Beard, 2011). The conversion of absorbed optical energy, H, to heat can be defined

$$H(r) = \mu_a(r)\Phi(r; \mu_a, \mu_s, g) \tag{2.1}$$

where μ_a is the local absorption coefficient at location r, and $\Phi(r; \mu_a, \mu_s, g)$ is optical irradiance at that location. The absorption and scattering coefficients, μ_a and μ_s,

respectively, correspond to optical properties of the tissue, and the anisotropy factor of the tissue is g.

Assuming impulsive heating, the initial pressure distribution p_0 can be related to the absorbed optical energy by

$$p_0 = \Gamma H(r) = \Gamma \mu_a(r) \Phi(r; \mu_a, \mu_s, g) \tag{2.2}$$

where the Grüneisen coefficient is defined $\Gamma = \frac{\beta c^2}{C_p}$. This thermodynamic constant describes the efficiency of converting from heat energy to pressure by relating the speed of sound c, the specific heat capacity C_p, and the volume thermal expansivity β of the tissue. We can see from Equation 2.2 that both p_0 and Φ depend on μ_a, therefore the amplitude of a PA wave depends nonlinearly on μ_a, an important factor when attempting to quantify spectroscopic properties of chromophores using PA techniques (Beard, 2011).

2.1.3   Confinement Conditions

Equation 2.2 assumes that thermal conduction and stress propagation are negligible during the laser pulse. The pulse width of the source laser, τ_p, must be shorter than both the time for heat dissipation of the absorbed energy τ_{th}, and the time for stress to pass the heated region τ_s. The former is known as the thermal confinement condition, where heat diffusion can be neglected; and the latter the stress confinement condition, which ensures a rapid buildup of thermoelastic pressure (Xu and Wang, 2006).

Considering a sample with a thermal diffusivity D_T, we can define the time for

thermal diffusion

$$\tau_{th} \sim \frac{L_p^2}{4D_T} \tag{2.3}$$

where L_p is a representative linear dimension, such as the size of the absorbing target or depth of penetration of the source beam. The time for stress to pass the heated region is defined

$$\tau_s = \frac{L_p}{c} \tag{2.4}$$

where c is the speed of sound in the medium. Summarily, the source pulse width must meet the following conditions (Gusev and Karabutov, 1993)

$$\tau_p \ll \frac{L_p^2}{4D_T} \quad \& \quad \tau_p < \frac{L_p}{c} \tag{2.5}$$

In general, a source beam with a pulse width in the nanosecond range is used, which easily meets these conditions for spatial resolution on the order of hundreds of micrometers in human tissue (Xu and Wang, 2006).

2.1.4 Laser-Ultrasound Propagation

At wavelengths beyond about 1000 nm, water has a strong absorption coefficient. A majority of human tissue is composed of water, therefore strong absorption occurs at the surface of the tissue when source lasers beyond the optical window are used. The laser-ultrasound (LU) wave that is generated at the surface then propagates through the tissue as in traditional ultrasound imaging. Through careful analysis of the path of this wave, an ultrasound image can be reconstructed. While PA image contrast is dominated by optical absorption and mechanical and thermodynamic quantities are typically neglected, LU images provide information about mechanical contrast.

Stenosis and calcification detection are examples of valuable information that can be obtained through analysis of the LU wave, which are not readily extracted from PA imaging. As a result, the use of a dual PA-LU system can provide a wealth of information about tissue constituents.

The simplified wave equation for acoustic wave propagation in human tissue is dictated by the differential equation defined as

$$(\frac{\partial^2}{\partial t^2} - c^2 \Delta^2)p = \Gamma \frac{\partial H}{\partial t} \tag{2.6}$$

This equation assumes the confinement conditions of Equation 2.5 have been satisfied, the acoustic pressure is substantially lower than conventional ultrasound pressure (in the kPa range), and the tissue is homogeneous (Beard, 2011; Wang, 2009).

2.1.5   Limitations of Photoacoustic and Laser-Ultrasound Imaging

The primary limitations of photoacoustic and laser-ultrasound imaging relate to probing depth and spatial resolution. Attenuation is high for high frequency acoustic waves in tissue, therefore high resolution images are known to sacrifice depth penetration. Likewise, visualizing deep structures in tissue results in a loss of resolution. While this is a known limitation for ultrasound imaging, the greater limitation for PA imaging is optical attenuation due to the strong scattering of light in human tissue.

Additional limitations include slow data acquisition times because of the low repetition rates of the source laser, imperfect image reconstruction algorithms, and design of the acoustic detector, which will be discussed in more detail in Chapter 3.

CHAPTER 3:

ACOUSTIC WAVE DETECTION METHODS

Methods of detecting acoustic waves for medical imaging are described in this chapter. The characteristics, advantages, and disadvantages of traditional ultrasound transducers for both ultrasound and photoacoustic detection are discussed. Subsequently, the basic theory of interferometric detection of acoustic waves, and the associated benefits and obstacles are presented.

3.1 Piezoelectric Transducers

Piezoelectric transducers are currently used for clinical ultrasound imaging. These contacting transducers have relatively narrow bandwidths, which requires the operator to choose the transducer with the most suitable range of frequencies for each application. Typically, transducers range from 1 MHz to 15 MHz. High spatial resolution is obtainable with high frequency transducers, however, only superficial structures can be detected due to strong high frequency attenuation in human tissue. With lower frequencies, deeper penetration is possible, at the sacrifice of spatial resolution. Ultrasound transducers are typically made of ceramic materials or polymers, which require contact with the sample to be imaged (Kihm *et al.*, 2009). A majority of photoacoustic imaging work is done with piezoelectric transducers, which leads to the possibility of combining photoacoustic and ultrasound imaging capabilities in a single instrument (Kim *et al.*, 2011, 2010).

Additional limitations arise for photoacoustic imaging with piezoelectric transducers. A majority of piezoelectric transducers are made from opaque, ceramic materials. As a result, delivering light to the tissue when access to the sample is limited to one side is a considerable design challenge (Zhang *et al.*, 2008). With further development, transparent detectors made of polyvinylidene fluoride have potential to overcome this problem (Niederhauser *et al.*, 2007). Furthermore, most reconstruction algorithms assume the use of point detectors. This requires each detector element to be smaller than the smallest structure to be imaged for accurate reconstruction. Sensitivity reduces significantly with decreasing element size, therefore imaging of small structures is problematic (Zhang *et al.*, 2008). Overall, environmental constraints, spatial resolution and frequency needs, and sample accessibility present obstacles for realizing the full potential of both photoacoustic and ultrasonic imaging using piezoelectric transducers (Balogun and Murray, 2011).

3.2   Optical Interferometry

Optical detection of acoustic waves using interferometry has distinct advantages over contacting transducers. Typically, interferometers have broadband frequency characteristics, allowing a wide range of frequencies to be detected, without requiring calibration. In addition, no acoustic contact with the sample is necessary (Kihm *et al.*, 2009). The ability to image safely, without contacting the patient, and without the need for personnel to manually control a transducer creates the potential for interferometry-based image detection to be advantageous in both clinical and surgical procedures. Lateral resolution is dependent on the spot size of the detection beam and the scanning capabilities of the stage for photoacoustic imaging, therefore

increased PA resolution is possible with interferometry detection (Kihm *et al.*, 2009).

The most common interferometers fall into two categories: wavefront splitting and amplitude splitting, the latter of which is typically used for the detection of acoustic waves (Hecht, 2002). Detection type, interference pattern, coherence of the light source, signal modulation, and geometrical configuration are additional characteristics used to classify interferometers (Kihm *et al.*, 2009).

For medical imaging purposes, interferometers are used to detect the thermoelastic response of a target by measuring surface displacement or particle velocity. In a simple interferometer, a laser beam is split into two arms: a reference beam and a probe beam, Figure 3.1. The reference arm has a known path length, and the probe beam is incident on the detection surface. When an acoustic wave propagates through the sample to the detection surface, a small surface displacement results, modulating the optical path length of the probe beam. The reference and probe beams are then recombined, and the interference pattern is analyzed to determine the change in optical path length (Kihm *et al.*, 2009; Hecht, 2002).

Mathematically, the energy of the reference and probe beams can be represented as $E_1 = a_1 e^{i\omega_1 t}$, and $E_2 = a_2 e^{i\omega_2 t + \frac{2\pi}{\lambda} d}$, where a_1 and a_2 are the electric field amplitudes and ω_1 and ω_2 are the angular frequencies of the corresponding beams, λ is the wavelength of the source, and d is the change in optical path length (Kihm *et al.*, 2009; Hecht, 2002). The resulting irradiance (intensity) from the superposition of the two recombined beams can be described

$$I = (E_1 + E_2)(E_1 + E_2)^* = a_1^2 + a_2^2 + 2a_1 a_2 cos\delta \qquad (3.1)$$

where $\delta = (\omega_1 - \omega_2)t - \frac{2\pi}{\lambda}d$. Total constructive interference occurs when $cos\delta = 1$, and
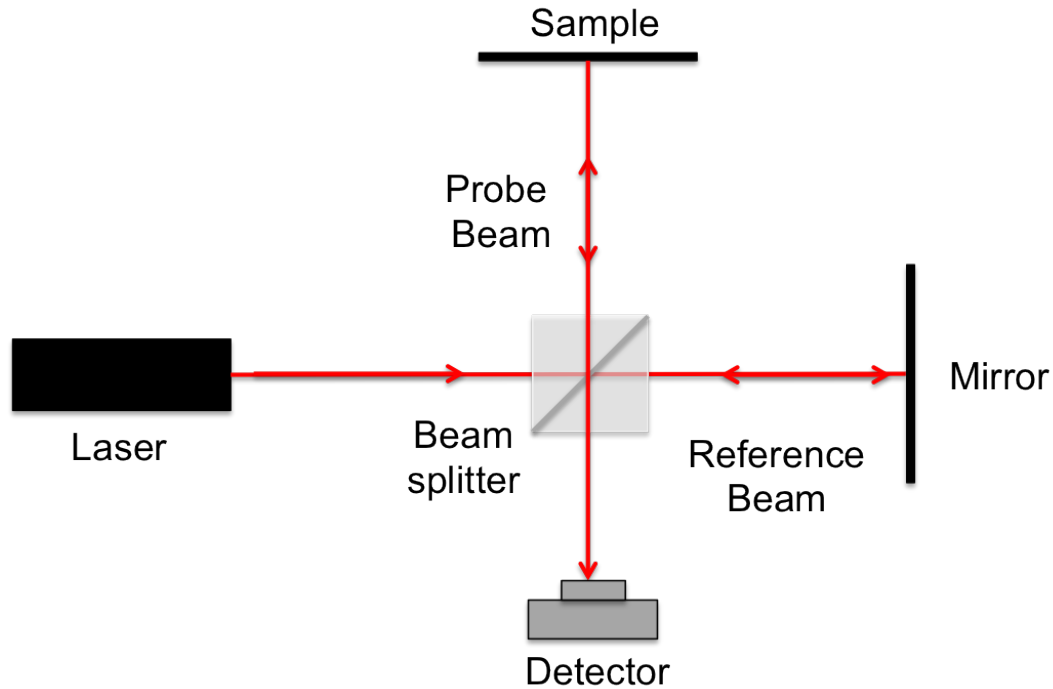
Figure 3.1: Simple Michelson interferometer. A source beam is split into a reference beam, with known path length, and a probe beam incident on the sample surface. When the two beams are recombined, the interference pattern is analyzed to determine the change in optical path length resulting from displacement of the probe beam by an acoustic wave.

the irradiance is a maximum. This maximum results when the disturbances are in-phase, or when the interference is an integer multiple of 2π. A minimum irradiance (total destructive interference) occurs when the waves are π radians out-of-phase ($cos\delta = -1$), which is represented as a trough in the interference pattern, Figure 3.2.

Both homodyne and heterodyne interferometers are considered amplitude-splitting interferometers, in which the amplitude of the beams in the two arms are lower than the original beam (Hecht, 2002). The general characteristic that differs between these two interferometers is the relationship between the optical frequencies of the reference and probe beam. In homodyne interferometry, $\omega_1 = \omega_2$, and $\delta = -\frac{2\pi}{\lambda}d$. The
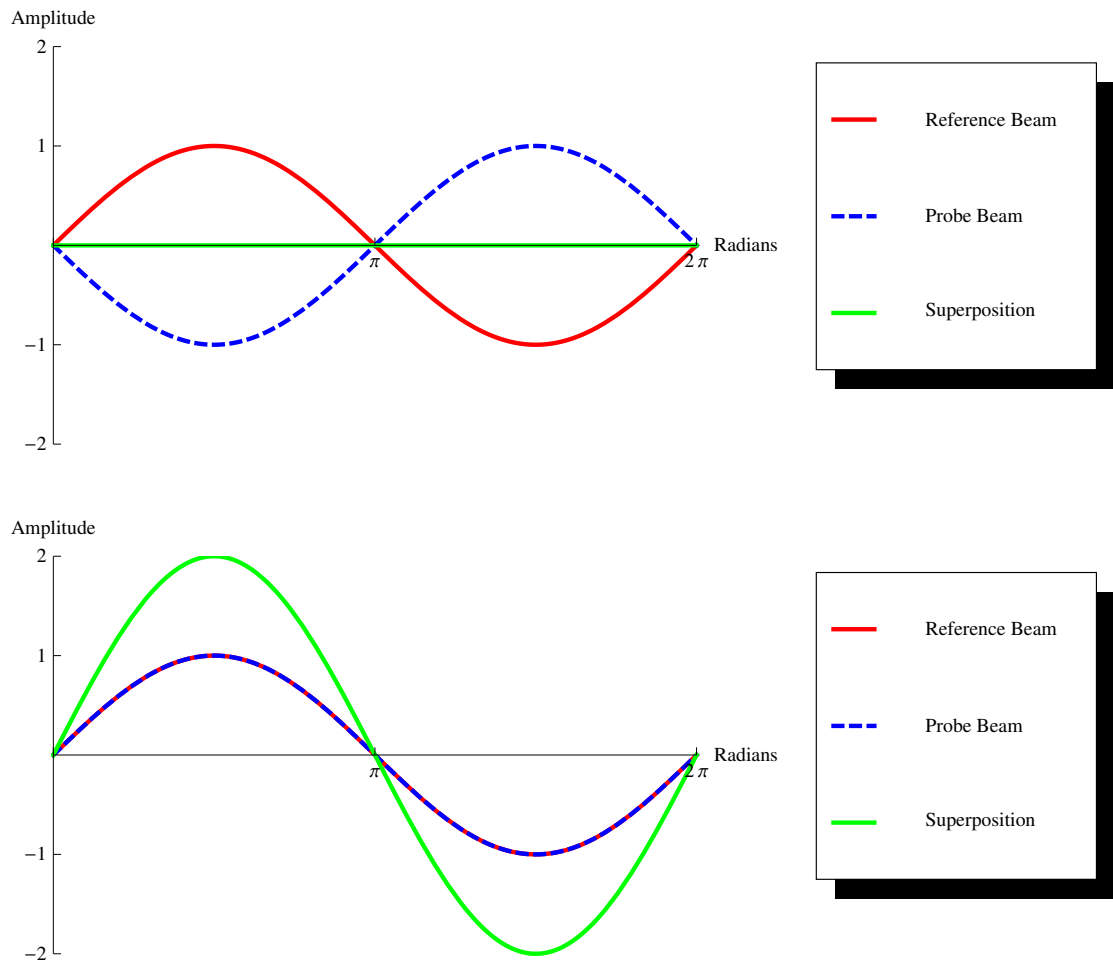
Figure 3.2: Top: total destructive interference of reference and probe beam, where $\delta = \pi$. Bottom: total constructive interference, where δ is an integer multiple of 2π.

well-known Michelson interferometer is an example of a homodyne interferometer. The optical frequency of one of the beams is modulated in heterodyne interferometry ($\omega_1 \neq \omega_2$). In this case, $\delta = \Delta\omega - \frac{2\pi}{\lambda}d$, where $\Delta\omega$ is the carrier frequency (Kihm *et al.*, 2009). Traditionally, heterodyne interferometers have been thought to be superior systems due to signal intensity sensitivity, non-continuous detection issues, and difficult alignment issues with homodyne systems. However, modern-day homodyne

interferometers have overcome many of these limitations. In our laboratory, we have used both homodyne (Bossa Nova Technologies, Tempo) and heterodyne interferometers (Polytec, PSV-400-M4) with success.

In general, interferometers require smooth, reflective surfaces for adequate sensitivity. To account for this, most experiments incorporate a reflective coupling medium, such as water or oil to smooth the sample surface and improve reflectivity.

CHAPTER 4:

PHOTOACOUSTICS IN MEDICAL IMAGING: STATE OF THE ART

This chapter provides an overview of recent photoacoustic imaging research toward characterization of atherosclerotic plaques. Strides toward photoacoustic detection of hemoglobin, lipids, and inflammation show promise for using photoacoustic imaging to visualize molecular constituents of plaque. Remote, optical detection of acoustic waves for biomedical applications is also under investigation, which has demonstrated improved resolution and increased detection bandwidth.

Room for improvement remains in obtaining high-resolution, deeply penetrating images, non-invasively, to increase the potential for screening patients for atherosclerosis and other vascular complications. Specifically, mechanical factors such as wall thickening, stenosis, and calcification have yet to be explored in depth with laser-generated ultrasound modalities. Non-invasive, safe imaging for treatment and surgical planning are additional motivations for improving depth and resolution using external detection methods. Improved image reconstruction and methods for clear, comparative analysis of contrast may also improve interpretation of PA and LU images.

4.1 Photoacoustic Imaging of Vascular Structures

The marked potential for distinguishing molecules based on spectroscopic properties using photoacoustic imaging has been described extensively (Wang, 2009; Xu and Wang, 2006; Beard, 2011; Laufer *et al.*, 2010). Visualization of vascular structures using photoacoustic techniques is advantageous because hemoglobin possesses unique spectroscopic properties within the optical tissue window (700 - 900 nm), where penetration of multiple centimeters is possible (Xu and Wang, 2006). Within this window, the absorption coefficient of hemoglobin is up to six orders of magnitude higher than surrounding tissue constituents, allowing for high contrast images with virtually nonexistent background noise (Wang, 2009).

Photoacoustic imaging of lipid pools in atherosclerotic plaque is beginning to be explored. By exploiting the unique spectroscopic properties of lipid molecules, Allen *et al.* (2012) imaged the full thickness of a plaque lesion in the wall of a human aorta with excellent signal-to-noise ratio. Identifying calcium deposits, however, is not as readily achieved through this spectroscopic photoacoustic imaging technique, as the spectral properties of calcium are indistinct in the range of 700 to 1400 nm. Through an indirect method, however, Kang *et al.* (2011) were able to image breast microcalcifications as small as 50 μm ex vivo. Excitation wavelengths between 690-700 nm were found to be optimally absorbed by calcifications. However, this range is strongly absorbed by hemoglobin molecules as well, creating a significant obstacle for vascular calcification detection using spectroscopic techniques. The inflammatory response of atherosclerotic lesions has also been investigated using photoacosutic molecular imaging with gold nanorods as a targeting agent (Ha *et al.*, 2011; Yeager *et al.*, 2012; Kim *et al.*, 2007).

The attenuation of high-frequency ultrasound waves has been a driving factor for the development of intravascular ultrasound and intravascular photoacoustic imaging (IVPA) techniques to evaluate atherosclerotic lesions with high resolution. The feasibility of differentiating several constituents of atherosclerotic plaque using combined IVUS and IVPA imaging probes has been demonstrated with high axial resolution (Sethuraman *et al.*, 2005). Detectors with frequency ranges of up to 80 MHz have been developed, allowing for structures as small as 6 μm to be detected (Li *et al.*, 2012b). Recently, lipids were visualized ex vivo using ultrasound guided IVPA in rabbit and human specimens (Wang *et al.*, 2012). In each of these experiments, high resolution was obtained, yet the invasive nature and limited depth penetration remain drawbacks to intravascular techniques (Wang, 2009).

4.2 Remote Photoacoustic and Laser-Ultrasound Imaging

Noncontact photoacoustic and laser-ultrasound detection is growing and continually increasing in sophistication. Photoacoustic imaging experiments have been accomplished using both homodyne and heterodyne interferometers, with some of the first experiments occurring as early as ten years ago (Payne *et al.*, 2003). Carp *et al.* (2004) detected polyamide tubes smaller than 200 μm using a modified Mach-Zehnder interferometer; however, an arcing artifact is evident, intrinsic to the delay and sum beamforming algorithm used. Similarly, a Mach-Zehnder interferometer has been used as a line-detector to obtain three-dimensional photoacoustic images with resolutions of less than 300 μm (Paltauf *et al.*, 2007b; Holotta *et al.*, 2011). Unlike traditional

interferometers that measure phase changes in a probe beam perpendicular to the sample, this detector beam is directed parallel to the sample surface. Reconstruction was accomplished by first calculating a linear projection of the detector line across the object surface and rotating the detector array, and applying a final Radon transform reconstruction (Paltauf *et al.*, 2007b). Radon transforms reconstruct an image by computing a line integral for each trace recorded in time at an offset position. Subsequent experiments incorporate a faster time-domain reconstruction algorithm, yet with both frequency and time domain approaches, smearing of the object edges is evident due to a limited view problem (Paltauf *et al.*, 2007a). An acoustic mirror was also incorporated to increase sensitivity using this method. Using an inverse Radon transform, enhanced sensitivity, with a resolution of 120 μm at superficial depths (10 mm) was achieved (Nuster *et al.*, 2012). In each line-detector experiment, the sample is immersed in water, for acoustic coupling of the waves to the probe beam.

A homodyne, low-coherence interferometer, equivalent to that used for traditional optical coherence tomography, was used by Wang *et al.* (2011) to image hair and blood vessels with resolution of less than 100 μm both axially and laterally. A mineral oil was used to improve system sensitivity to surface roughness. Both the source and detection beams were focused, which allowed for high resolution, but only superficial depths to be imaged (1.0 mm).

Most interferometers require detection on smooth surfaces, yet large étendue interferometers have increased sensitivity on rough surfaces, including confocal Fabry-Perot interferometers and two-wave mixing systems (Pouet *et al.*, 2011). Recently, Rousseau *et al.* (2012a, b) developed a fully-noncontacting PA and ultrasound imaging system that does not require a coupling medium. A confocal Fabry-Perot inter-

feerometer was used, which incorporated careful shaping of a pulsed detection beam. This allowed for the use of a high-energy detection beam, without exceeding the American National Standard Institute (ANSI) safety limits. After reconstructing the images using a synthetic aperture focusing technique, hyperbolic artifact remained due to improper focusing by the algorithm. A two-wave mixing interferometer with a photo-refractive crystal has also been applied to biomedical photoacoustic imaging. The interferometer used does not require a coupling medium, and has the capability to image on rough surfaces. With the implementation of a Fourier synthetic aperture focusing technique, structures as small as 120 μm at depths of 4 mm were detected in tissue-mimicking phantoms (Hochreiner *et al.*, 2012).

Air-coupled transducers have also been evaluated for noncontact photoacoustic signal detection. It was necessary for the transducer to be sufficiently close to the sample (7.5 mm detection distance), and both bandwidth and sensitivity limitations remain. Additionally, available air-coupled transducers are unfocused, limiting resolution (Kolkman *et al.*, 2010).

Fabry Perot polymer film interferometers have overcome many of the limitations described in Section 3.1, yet still require contact with the sample. Careful design of the film achieves optical transparency, so that the excitation beam can be transmitted directly through the sensor head. The additional characteristics of optical detection, including improved sensitivity and resolution, broadband frequency response, and straightforward backward mode detection schemes are advantages of this technique (Zhang *et al.*, 2011, 2008; Beard *et al.*, 2009).

Overall, photoacoustic imaging using remote detection techniques has gained increasing interest in recent years. Imaging capabilities and practicality are continuing

to improve, yet many obstacles remain. While resolution continues to improve for superficial structures, attenuation is a consistent limitation for accurate image reconstruction beyond about 1 cm. Additionally, hyperbolic artifacts remain in many images after reconstruction using traditional biomedical imaging algorithms. What's more, noncontact acoustic detection for biomedical applications has focused on photoacoustic detection, while the analysis of the LU wave generated at the surface is only beginning to be explored. Li *et al.* (2012a) describe the first experiment using laser ultrasound measurements to evaluate mechanical properties of a tissue-mimicking phantom, while the noncontact ultrasound images obtained by Rousseau *et al.* (2012a, b) are the first of their kind. Our motivation is to improve PA and LU resolution and clarity at depths beyond 1 cm using image processing techniques from seismology. In addition, a method of jointly analyzing contrast among absorbers and scatterers are expected to enhance interpretation of PA and LU images.

CHAPTER 5:

METHODS

5.1   Experimental Setup

In this chapter, experimental methods for obtaining PA and LU images using optical excitation and detection are presented. Phantoms were created to represent human tissue properties, with structures embedded that replicate characteristics of healthy and diseased vessels. Of particular interest is the difference in PA generation and LU scattering due to increased acoustic impedance of the vessel wall.

Image processing methods are also described, which were used to remove interfering waves, improve image contrast, and accurately locate absorbers and scatterers. Finally, a method of jointly analyzing photoacoustic and laser-ultrasound contrast is presented. All image processing was accomplished using MATLAB® software.

5.1.1   Phantom Construction

A solid tissue-mimicking phantom was constructed to simulate the optical scattering and acoustic properties of human tissue. The phantom was composed of 1% Intralipid®, 1% highly purified agar (A0930-05, USBiological), and deionized water. Intralipid® is a phospholipid emulsion that is widely used for optical and photoacoustic phantom studies because it is a homogeneous and turbid medium, without distinct absorption bands (Yao *et al.*, 2010; Flock *et al.*, 1992; Kinnunen and Myllylä, 2005; Driver *et al.*, 1989; Cubeddu *et al.*, 1997). Agar was used to solidify the phantom,

without notably increasing turbidity or absorption (Cubeddu *et al.*, 1997).

Several proxies were embedded into the phantom to mimic absorbing and scattering properties of vascular structures with varying compositions. A thin-walled polyester tube (1.57 mm inner diameter) was chosen to represent a non-diseased vessel. The tube was optically clear, so that it did not contribute to absorption, and therefore PA wave generation. The wall-thickness of the polyester tube (12.7 μm) was considerably smaller than the expected wavelength of the source, therefore it was assumed to be acoustically transparent. While the acoustic impedance of polyester is relatively high, it was negligible for the small thickness. In contrast, an acrylic tube with an inner diameter of 1.4 mm and wall thickness of 233.5 μm was used to represent a vessel that had increased acoustic impedance, such as an artery stiffened by calcification. Each of these surrogates was placed 18 mm below the surface of the phantom.

Table 5.1 shows the acoustic impedance and modulus of rigidity for each medium used. The fraction of the incident wave that is reflected at the interface between two mediums is defined by the reflection coefficient:

$$R = \frac{Z - Z_0}{Z + Z_0} \tag{5.1}$$

where Z and Z_0 are the acoustic impedance of the first medium (phantom) and second medium (artery surrogate), respectively. The value of R ranges from 0 to $\pm$ 1, where the amplitude of a reflected wave at an interface where $R = \pm$ 1 is equal to the amplitude of the incident wave. The reflection coefficients expected for each interface are recorded in Table 5.2.

An infrared absorbing dye (Epolight$^{\text{TM}}$ 2057) dissolved in isopropyl alcohol was

Medium	$\rho(\frac{kg}{m^3})$	$c(\frac{m}{s})$	$Z(\frac{MNs}{m^3})$	G (GPa)
Phantom	1000	1390	1.39	$\approx 10*10^{-6}$
Polyester	1400	–	–	0.9
Acrylic	1180	2740	3.23	1.7
Air	1.2	343	$4.12*10^{-4}$	0
Dye	786	1170	0.92	0

Table 5.1: Typical acoustic and mechanical properties of tissue phantom and embedded mediums, where ρ is the mass density, c is the speed of sound, Z is acoustic impedance, and G is the modulus of rigidity. The modulus of rigidity of the phantom was considered negligible relative to the tubes. In addition, the thin wall of the polyester tube (relative to the source wavelength) allowed for a negligible acoustic impedance. References used: (Bloomfield *et al.*, 2000; Selfridge, 1985; Pavan *et al.*, 2010).

Interface	R
phantom-air	-0.9994
phantom-dye	-0.2037
phantom-polyester	≈ 0
phantom-acrylic	0.4038

Table 5.2: Reflection coefficient R of interface between tissue phantom and embedded mediums. The acoustic impedance of the air-polyester interface was negligible because the wall thickness was acoustically transparent. A negative reflection coefficient corresponds to a 180° phase shift of the reflected wave.

used to represent a chromophore in the body. As a comparison, trials were accomplished with each tube filled with both air and dye. While the dye was chosen to absorb light at 1064 nm, air is optically transparent, and was not expected to generate a PA wave. In contrast, the acoustic impedance of air is significantly different than the acoustic impedance of the phantom, as the majority of the phantom was composed of water whereas alcohol in the dye more closely mimicked the acoustic impedance of the phantom. We therefore expected the LU scattering due to air to exhibit higher contrast than scattering from the dye. Likewise, the acrylic tube was

Tube type	None	Polyester (Healthy Vessel)		Acrylic (Calcified Vessel)	
Trial Number	1.	2.	3.	4.	5.
Tube Filling	–	Air	Dye (Blood, Lipids)	Air	Dye (Blood, Lipids)

Table 5.3: Summary of experiments. Trial numbers correspond to the type of tube embedded in the phantom and the "filling" within the tube. The tissue analogue that corresponds to each surrogate is labeled in parenthesis.

expected to scatter the LU waves, while the polyester tube's contribution to scattering was expected to be negligible.

A total of five trials were recorded, which allow for examination of PA wave generation, which provided spectroscopic information, and LU wave scattering, which gave insight to changes in acoustic impedance. These trials are listed in Table 5.3, and will be referenced by the corresponding trial numbers hereafter.

5.1.2 Laser System and Setup

As discussed in Section 2.1, rapid absorption of optical energy by an absorber generates a sound wave that can be detected at the phantom surface. In general, pulsed laser light is used to accomplish this task. For our experiments, we used a Neodymium-doped Yttrium Aluminum Garnet (Nd:YAG) laser with a wavelength of 1064 nm and nanosecond pulsing capabilities (QuantaRay, Spectra Physics, Newport Corporation, Irvine, California). An unfocused beam (8 mm diameter) was pulsed with a 10 ns pulse width and 11 Hz repetition rate. For a spatial resolution of at least 1.5 mm, the conditions from Equation 2.5 must be met. Assuming a thermal diffusivity of 1.4 X 10^{-3} cm^2/s for human tissue (Duck, 1990) and $c = 1500$ m/s, τ_p

must be less than 1000 ns, which was easily met using our pulse width of 10 ns. The pulse energy was kept at approximately 100 mJ/cm^2, but we recognize additional energy considerations will be required to keep the laser exposure below the American National Standard Institute maximum permissible exposure for repetitive pulses at 1064 nm. A scanning heterodyne interferometer (vibrometer) was utilized for detection of the PA and LU waves (Polytec PSV-400-M4). Line scans were recorded in reflection mode, where the detection beam was scanned by 336.9 μm increments away from the location of the source beam, with an average of 64 A-scans recorded per beam location. A total of 95 traces were recorded, covering a scan distance of 3.2 cm.

The source beam was incident on the phantom surface, to allow penetration of the laser light into the phantom. A reflective tape was placed across the detection surface for improved reflectivity and signal detection, Figures 5.2 and 5.1. The source wavelength is also strongly absorbed by water, which accounts for a majority of the composition of both human tissue and our phantom. The laser energy was thus absorbed by the phantom at the surface, generating an LU wave that propagated through the phantom.

5.2 Data Processing

5.2.1 Frequency Domain Filtering

Filtering in the frequency domain is a commonly used method for removing a particular range of frequencies from an image. In general, the process begins by computing the two-dimensional Fourier transform of an image, labeled F. The unwanted fre-
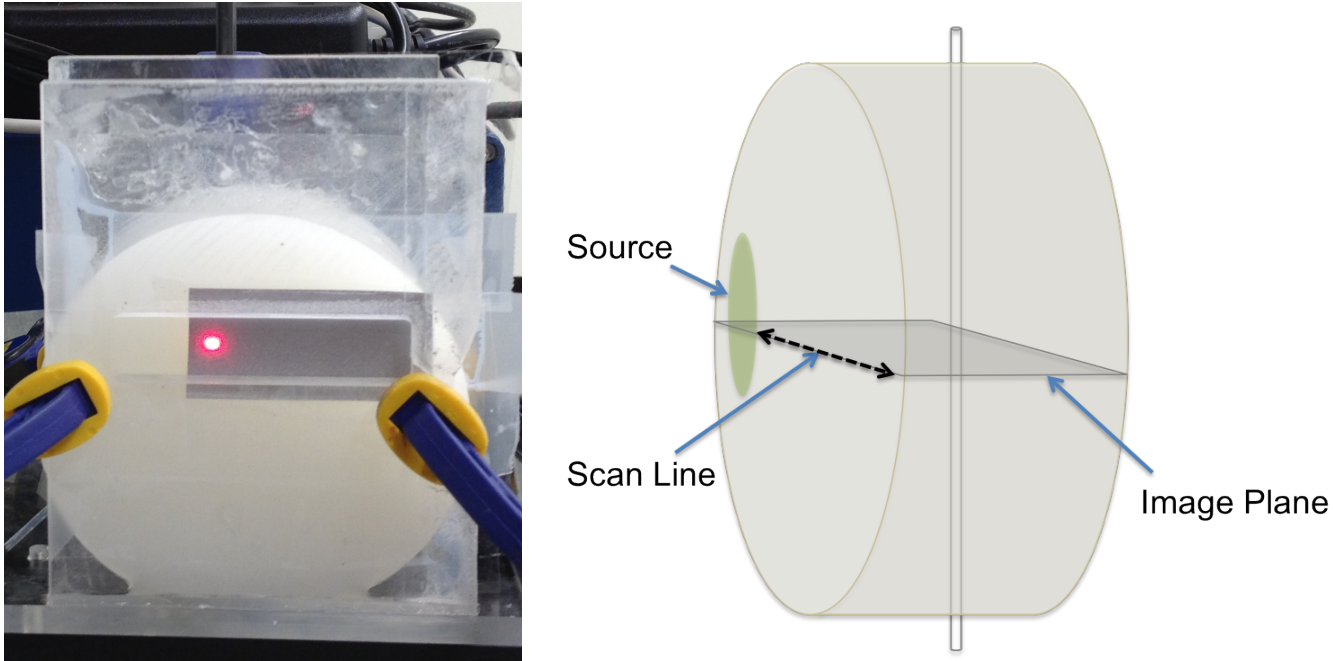
Figure 5.1: (a) Photograph of experimental setup, with the scan line shown. (b) 3D perspective view of phantom setup with 2D image plane shown.

quencies are "blocked out", and then the inverse transform is computed to reconstruct the image in the spatial domain.

In the case of an image that only varies with time in one dimension, the design of the filter is straight forward. We used a simple highpass filter H that set all frequencies below a defined cutoff f_c to 0, and 1 elsewhere:

$$H(f) = \begin{cases} 0, & \text{if } f < f_c, \\ 1, & \text{if } f \geq f_c, \end{cases} \tag{5.2}$$

A sharp edge in the frequency domain relates to a sinc function in the time domain, therefore we applied a common Butterworth smoothing function to the edges of the
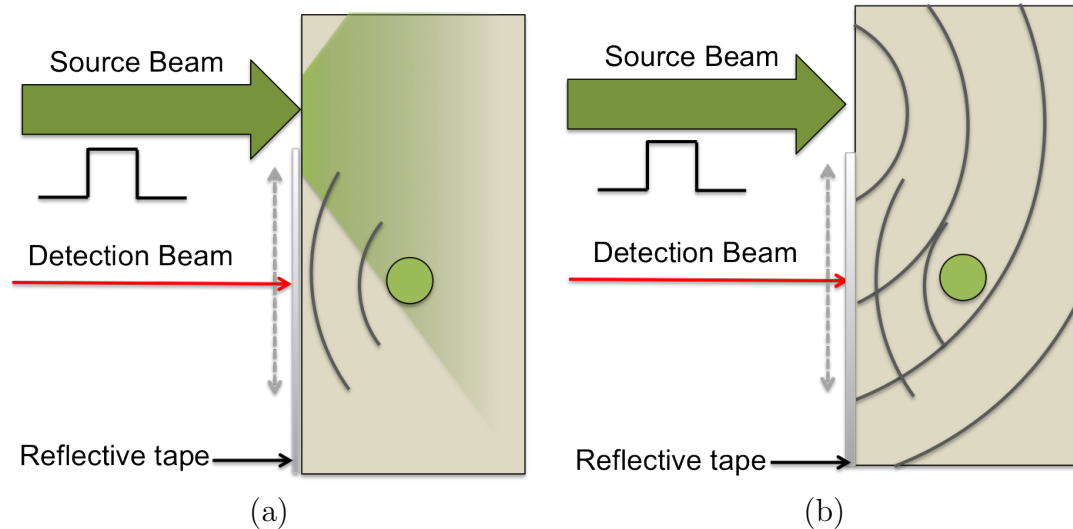
Figure 5.2: Diagram of (a) PA wave generation and (b) LU generation and scattering in the transverse plane of the phantom. In (a), the optical energy of the source beam is shown illuminating an absorber embedded in the phantom. This caused a PA wave to be generated, which was detected at the phantom surface. An LU wave was generated at the surface of the phantom as shown in (b). The deflection of this wave by a scatterer in the phantom was detected at the phantom surface. Both (a) and (b) occur concurrently, in a single scan.

filter to reduce ringing effects (Gonzalez and Woods, 2008). Multiplying H by F and computing the inverse Fourier transform resulted in the original image with the unwanted frequencies removed.

5.2.2   F-k Filtering

When an excitation laser that absorbs water is used for photoacoustic imaging, a wave is generated at the surface of the tissue, as described in Section 2.1.4. This causes a

wave to propagate not only through the tissue thickness, but also directly from the incident location of the source to the receiver, along the surface of the tissue. This direct wave can cause unwanted interference with the detection of waves generated or scattered within the tissue. Frequency-spatial frequency (f-k) filtering is a method that has successfully extinguished or suppressed waves in seismic images for decades (Hayashi and Sato, 2010; Bing *et al.*, 2011). F-k filters are often called velocity filters, which are used to separate waves that arrive from different directions (Hayashi and Sato, 2010). Generally, these filters are designed to suppress data in a particular region of the f-k domain.

A commonly used f-k filter is the pie-slice filter. Figure 5.3 shows a representative f-k spectrum and slowness (velocity^{-1}) lines with slopes $s_1 = k_1/f_1$ and $s_2 = k_2/f_2$. The region between two slowness-lines is suppressed in a pie-filter, where the filter k-width increases with increasing frequency (Mars *et al.*, 1997).

For this work, a pie-filter was designed to remove the direct wave in the f-k domain. The slopes of the slowness lines were carefully chosen by inspection of the f-k spectrum to suppress only the direct wave. A taper function was incorporated to smooth edges of the pie-filter, and reduce ringing effects from converting sharp edges in frequency space back to the time domain. The filter function used was defined:

$$H(f_x, k_x) = \begin{cases} 0, & \text{if } s_1 \leq s \leq s_2, \\ 1 - e^{-\left|\frac{s-s_1}{s_1}\right|^2}, & \text{if } s < s_1, \\ 1 - e^{-\left|\frac{s-s_2}{s_2}\right|^2}, & \text{if } s > s_2 \end{cases} \tag{5.3}$$

where the slowness at a given point in f-k space is $s(f_i, k_i) = \frac{k_i}{f_i}$.
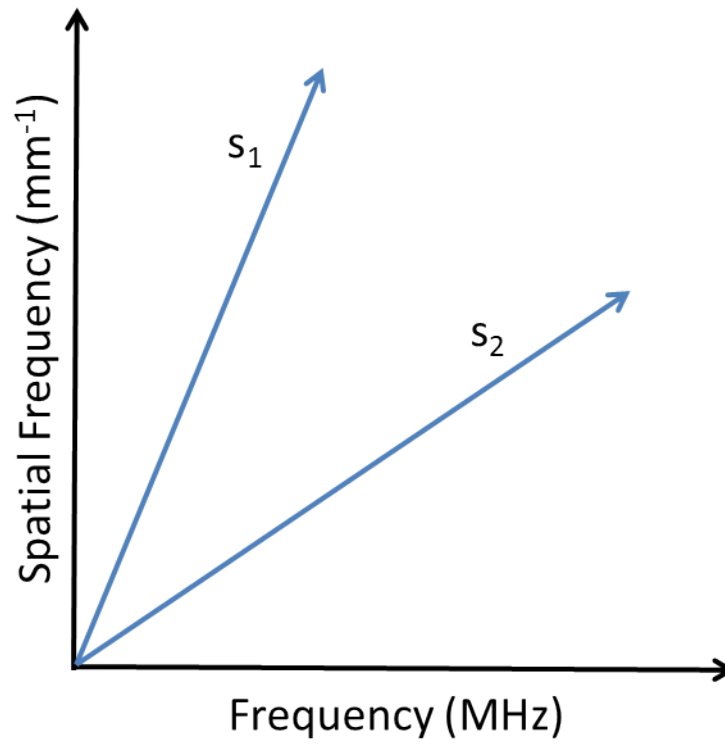
Figure 5.3: Diagram of f-k domain, with slowness lines having slopes equal to $s_1 = k_1/f_1$ and $s_2 = k_2/f_2$.

5.2.3   Normal Moveout Correction and Stacking

For our experimental set-up, we utilized a single source and multiple detector positions. Therefore, there was a difference between the time of arrival of waves detected in traces (A-scans) offset from the source with respect to waves recorded at zero offset. Seismologists remove this increased travel time using a normal moveout (NMO) correction (Dunkin and Levin, 1973; Rupert and Chun, 1975). This method uses knowledge about the offset between source and receiver x, wave travel time t, and wave speed c, to transform the traces and remove the increased travel time due to offset. Both x and t were known from the raw data and experimental parameters, which left c as a free parameter. The equation for a hyperbola, Equation 5.4, was used to calculate the difference in travel time between waves arriving at an offset, to a wave that arrived at zero offset, t_0

$$t^2 = t_0^2 + \frac{x^2}{c^2} \tag{5.4}$$

As shown in Figure 5.4, the travel time increased for a wave detected at an increased offset. More precisely, the time of arrival of both PA and LU waves increased hyperbolically with increasing offset from the source (PA) or scatterer (LU).

The time for an electromagnetic wave to travel from source to absorber was considered instantaneous in comparison to the time for an acoustic wave to travel the same distance. For a PA wave, originating in the absorber, the simple hyperbola equation was adequate. However, the time of arrival of an LU wave contains an additional offset because of the increased time for the LU wave to travel from source to scatterer. The travel time from source to scatterer t_1, and from scatterer to the
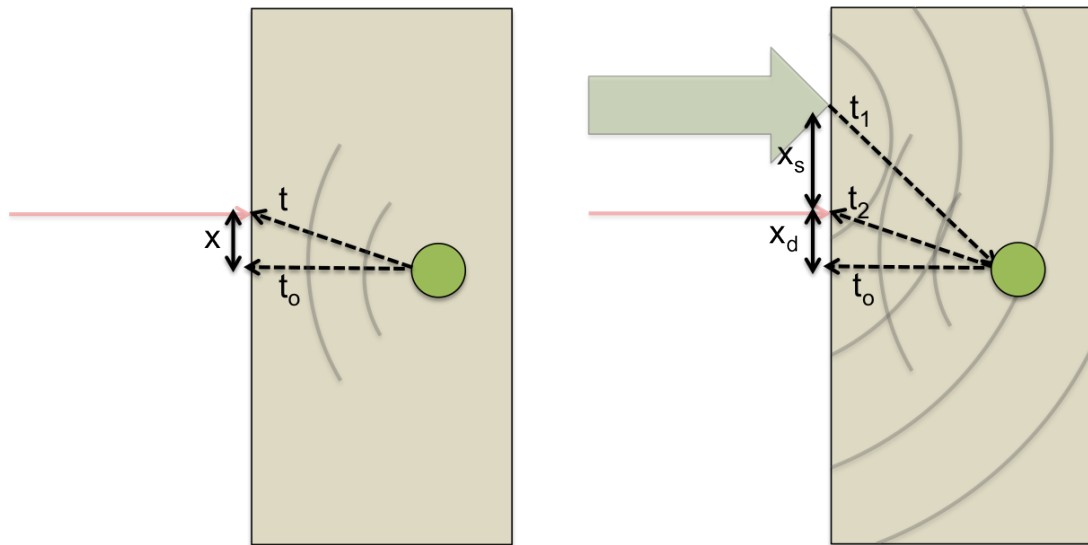
Figure 5.4: Propagation of acoustic waves. Left: diagram of actual travel time t for a PA wave that traveled to a detector offset a distance x from zero-offset. The travel time of a PA wave detected at zero offset was defined t_0. Right: travel time of an LU wave from source to scatterer t_1 and scatterer to surface t_2. The distance traveled for a wave originating at the scatterer and detected at zero offset is labeled t_0. The offset from source to detector x_s, must also be accounted for in the LU correction.

detector t_2 are related to account for the total LU travel time:

$$t = t_1 + t_2 \tag{5.5}$$

Likewise, an additional offset term x_s was added to the detector offset to account for the offset of the source with respect to the detector when calculating t_1, Figure 5.4(b), which is defined:

$$x = x_d + x_s \tag{5.6}$$

where x_d is the distance from zero-offset to the detector position. Substituting Equation 5.5 and 5.6 into Equation 5.4, the normal moveout was applied to LU scattered waves.

After the normal moveout was applied, a stacking procedure was implemented to enhance contrast, optimize c, and improve signal-to-noise ratio. All adjacent A-scans were summed together into a single trace and normalized. Semblance, a measurement of coherence among traces after NMO correction, was then evaluated. Many methods of analyzing semblance have been explored. For our processing, we defined semblance as the ratio of maximum amplitude of the wave of interest to amplitude of the noise in the stacked trace. The velocity in Equation 5.4 was varied until maximum semblance was achieved. This occurred when the same wave in adjacent traces summed constructively. The velocity at optimum semblance was an accurate measurement of the speed of sound in the medium, and the resulting stacked-trace was then used as an objective measure to relate contrast between trials.

CHAPTER 6:

RESULTS AND DISCUSSION

This chapter outlines the experimental results and processed images outlined in Chapter 5. The acquired, normalized images are shown in Figure 6.1. Both PA (Trials 3 and 5) and LU (Trials 2 - 5) waves were evident, however the relative contrast of each wave was unclear, and low frequency waves dominated the data. Additionally, the time of arrival of the direct wave, traveling from source to receiver, overlapped the arrival of the PA waves. As discussed in Section 5.2.3, the time of arrival of waves both generated in and scattered by the targets within the phantom increased hyperbolically as offset of the detector increased on either side of the tube. Using techniques native to geophysical image processing, described in Section 5.2, the interfering waves were suppressed and the hyperbolic time of arrival was corrected.

6.1   Image Filtering

The f-k spectra for each trial is shown in Figure 6.2. Two common features were present in each spectra: a distinct vertical line centered around the origin, representing abundant low frequency content, and a diagonal line through the origin, which indicated the unique slowness slope of the direct wave, as labeled in Figure 6.2(a). In order to remove these features, we applied the frequency domain and f-k filtering techniques described in Sections 5.2.1 and 5.2.2, respectively.

The wave generated at the surface of the phantom not only traveled throughout

(a) Trial 1

Air

Acoustic Contrast Agent

Dye

Molecular Absorber

**No
Tube**

**Polyester
Tube**
Healthy
Artery
Surrogate

**Acrylic
Tube**
Calcified
Artery
Surrogate

(b) Trial 2 (c) Trial 3

(d) Trial 4 (e) Trial 5
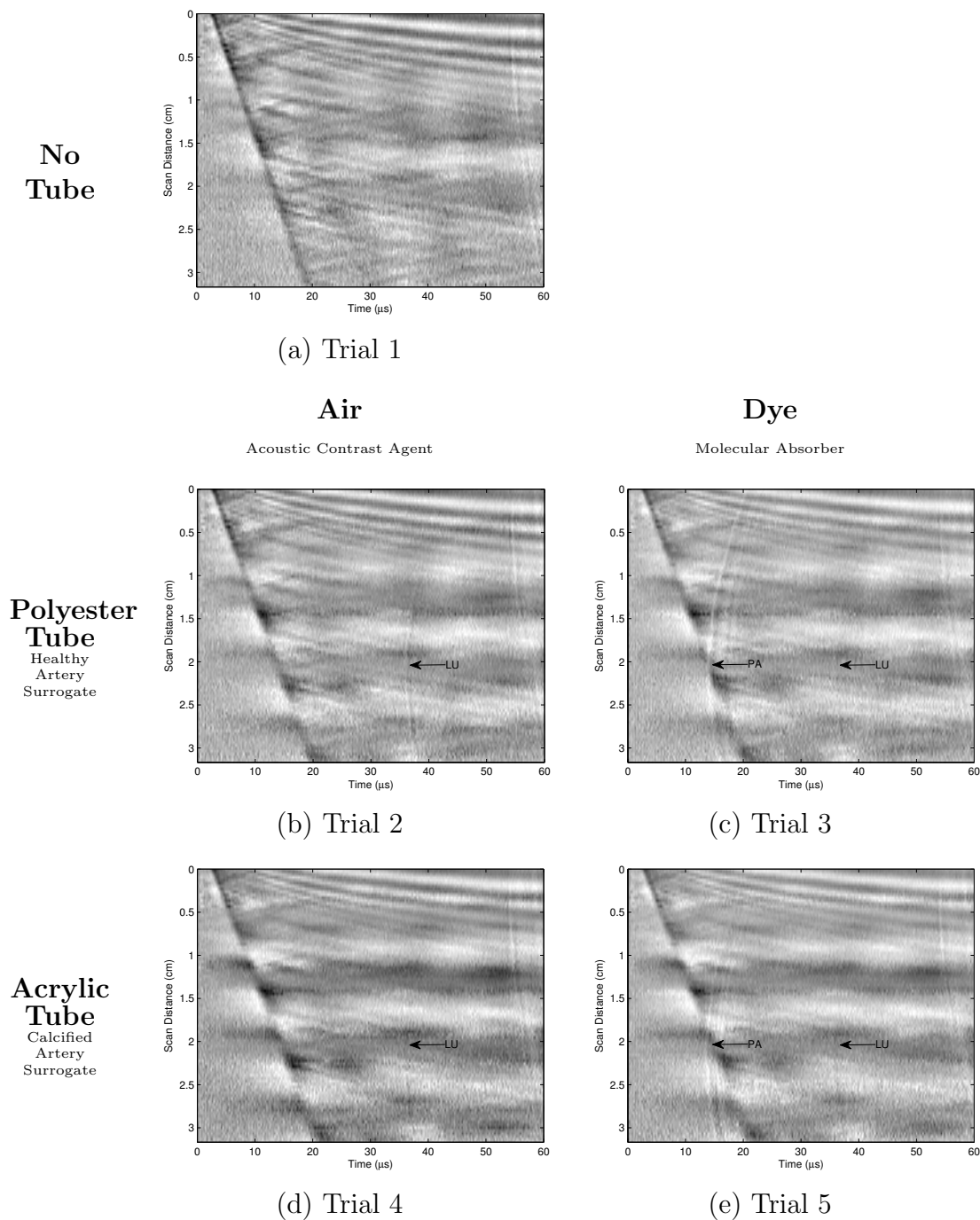
Figure 6.1: Normalized B-scan images in the time domain. The generated PA wave
and scattered LU wave are labeled for each trial at the location of the tube. The
direct wave and low frequency content overshadow the PA and LU waves. The time
of arrival for each wave increases hyperbolically with distance from the tube.

(a) Trial 1

Air

Acoustic Contrast Agent

Dye

Molecular Absorber

No Tube

Polyester Tube
Healthy Artery Surrogate

Acrylic Tube
Calcified Artery Surrogate

(b) Trial 2

(c) Trial 3

(d) Trial 4
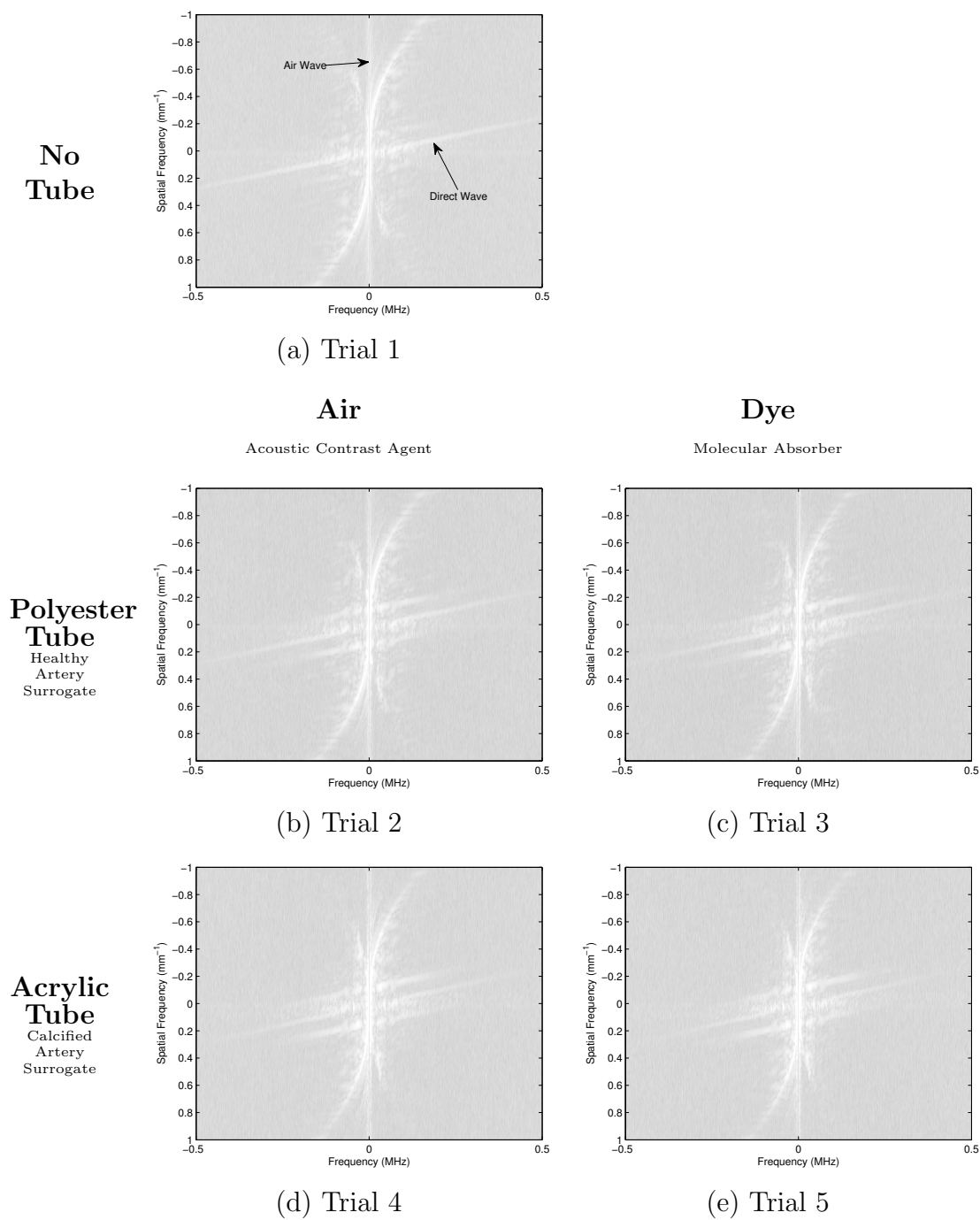
(e) Trial 5

Figure 6.2: F-k spectra for Trials 1-5. The direct wave and concentrated low frequency content are labeled in Trial 1 (a), with the phantom only.
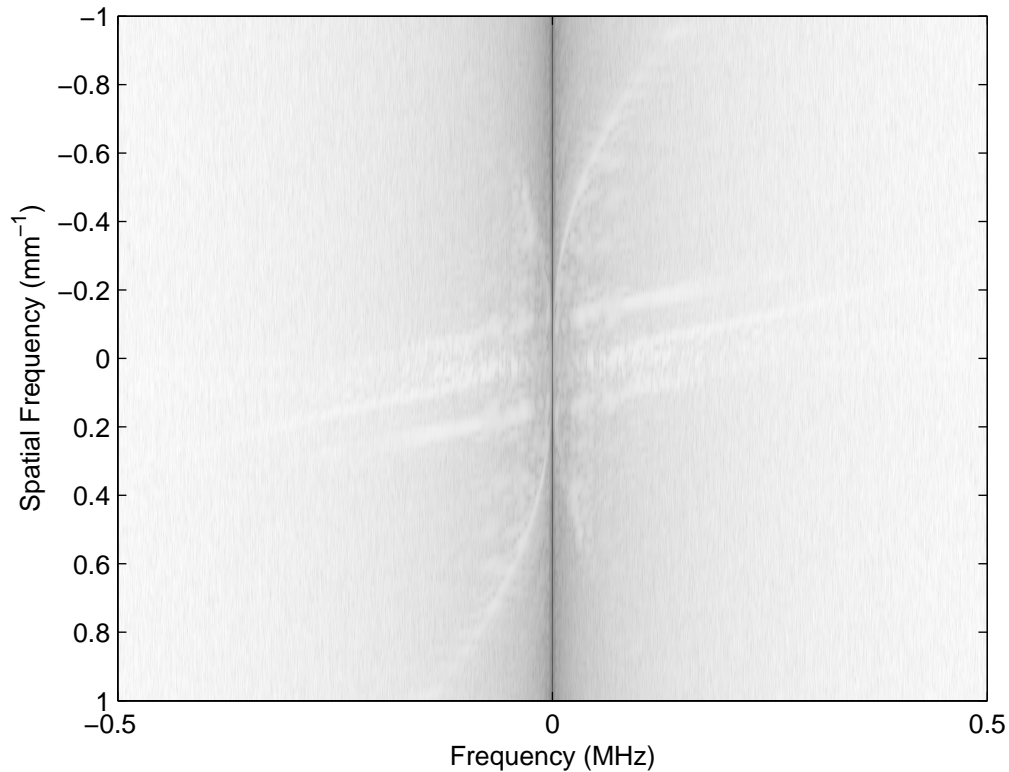
Figure 6.3: F-k spectra for Trial 5, with acrylic tube filled with dye. The information corresponding to frequencies below 100 kHz was suppressed by multiplying the f-k spectra by a filter that is zero for low frequencies.

the phantom, but a wave also propagated through the air along the phantom surface. The speed of sound through air is in the range of 350 m/s; significantly slower than the speed of sound through the phantom. Thus, this wave was easily removed using a highpass filter. The filter was designed as a first order Butterworth filter with a cutoff frequency of 100 kHz, as defined by Equation 5.2. The filtered spectra for Trial 5 is shown in Figure 6.3, and all highpass filtered images are shown in Figure 6.4.

After removing the air wave, an f-k filter was designed using Equation 5.3 to remove the direct wave. The slowness lines s_1 and s_2 were chosen in order to suppress

(a) Trial 1

Air

Acoustic Contrast Agent

Dye

Molecular Absorber

(b) Trial 2   (c) Trial 3

(d) Trial 4   (e) Trial 5
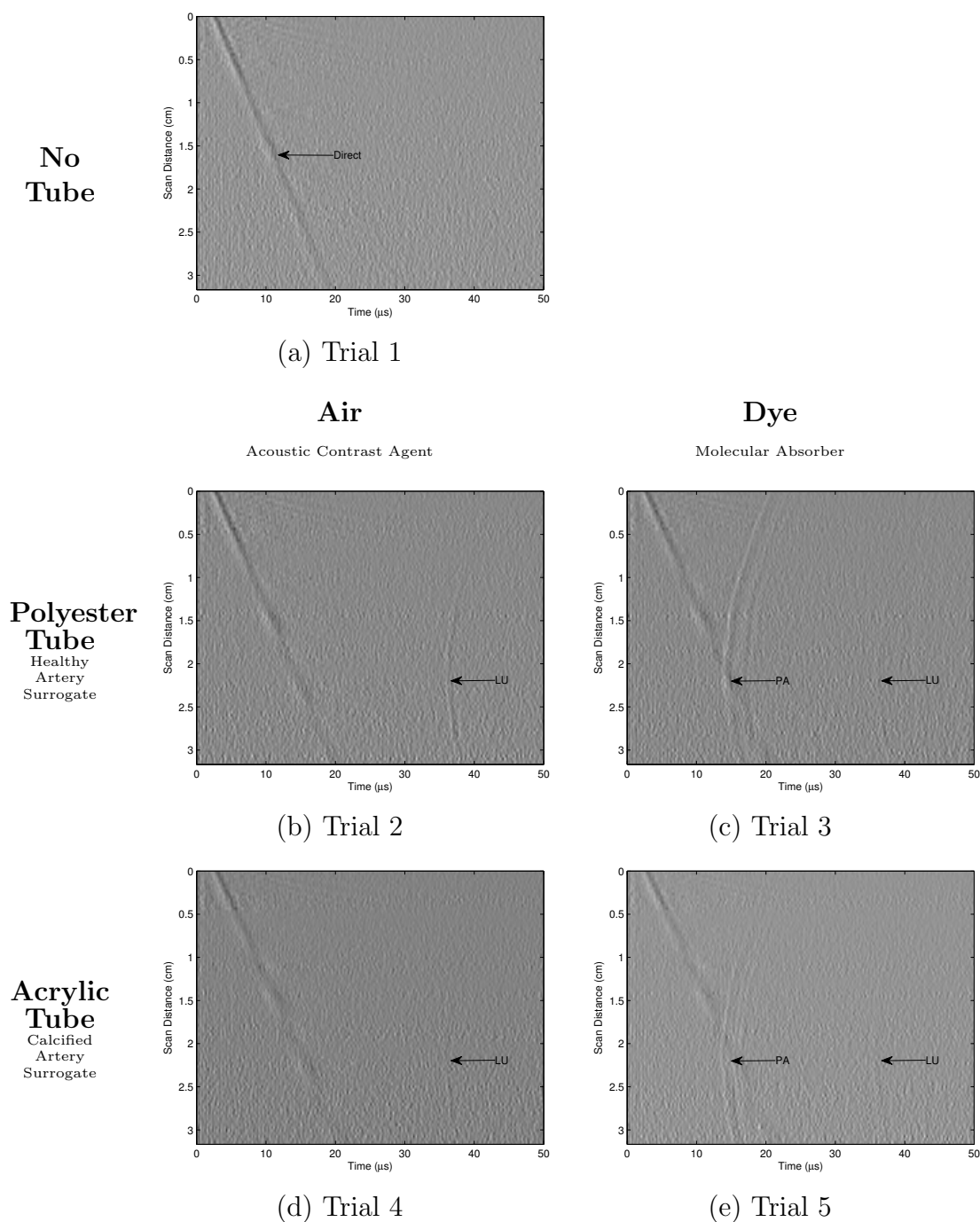
Figure 6.4: B-scan images for Trials 1-5 with low frequencies removed by a highpass filter. The direct wave interferes with the PA waves in (c) and (e).
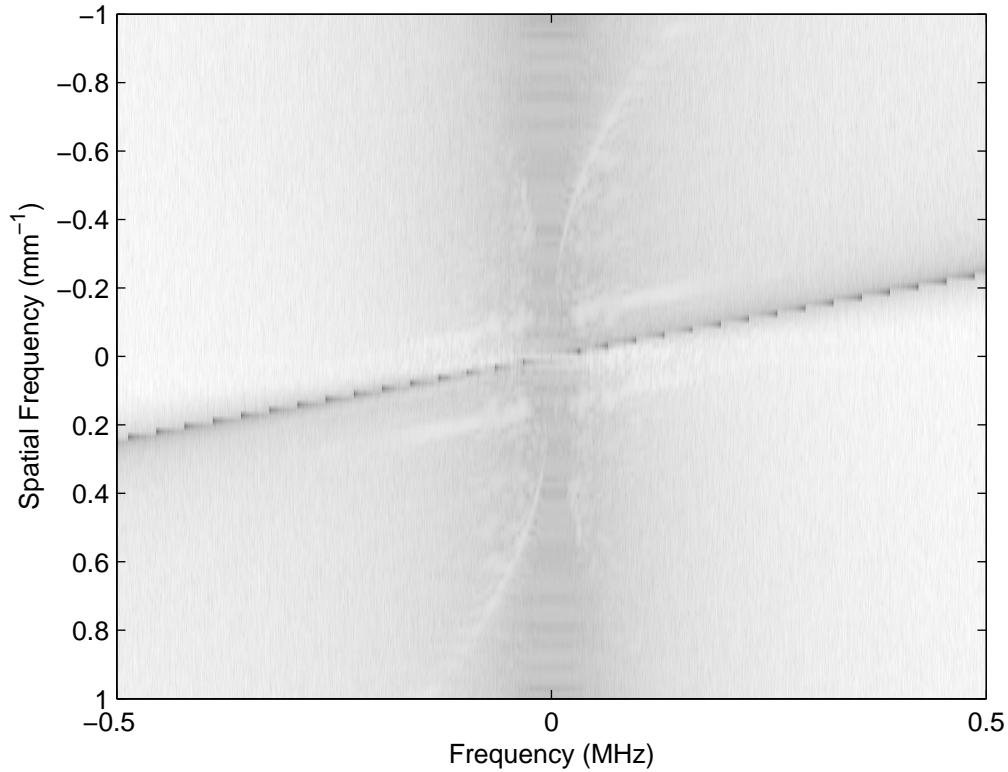
Figure 6.5: F-k spectra for Trial 5, with acrylic tube filled with dye. The direct wave spectra was suppressed by multiplication of the f-k spectra by a pie-slice filter.

the direct wave, without obstructing f-k information corresponding to the arrival of a PA or LU wave. The filtered spectra for Trial 5 is displayed in Figure 6.5, along with the images from each trial with the direct wave successfully suppressed in Figure 6.6.

6.2   NMO Correction and Stacking

We applied the normal moveout correction to the filtered images to remove the increased time travel for waves detected offset from the tube. This placed the wave arrivals at the time they would arrive if the waves originated at the absorber (PA)

(a) Trial 1

Air

Acoustic Contrast Agent

Dye

Molecular Absorber

(b) Trial 2

(c) Trial 3

(d) Trial 4

(e) Trial 5
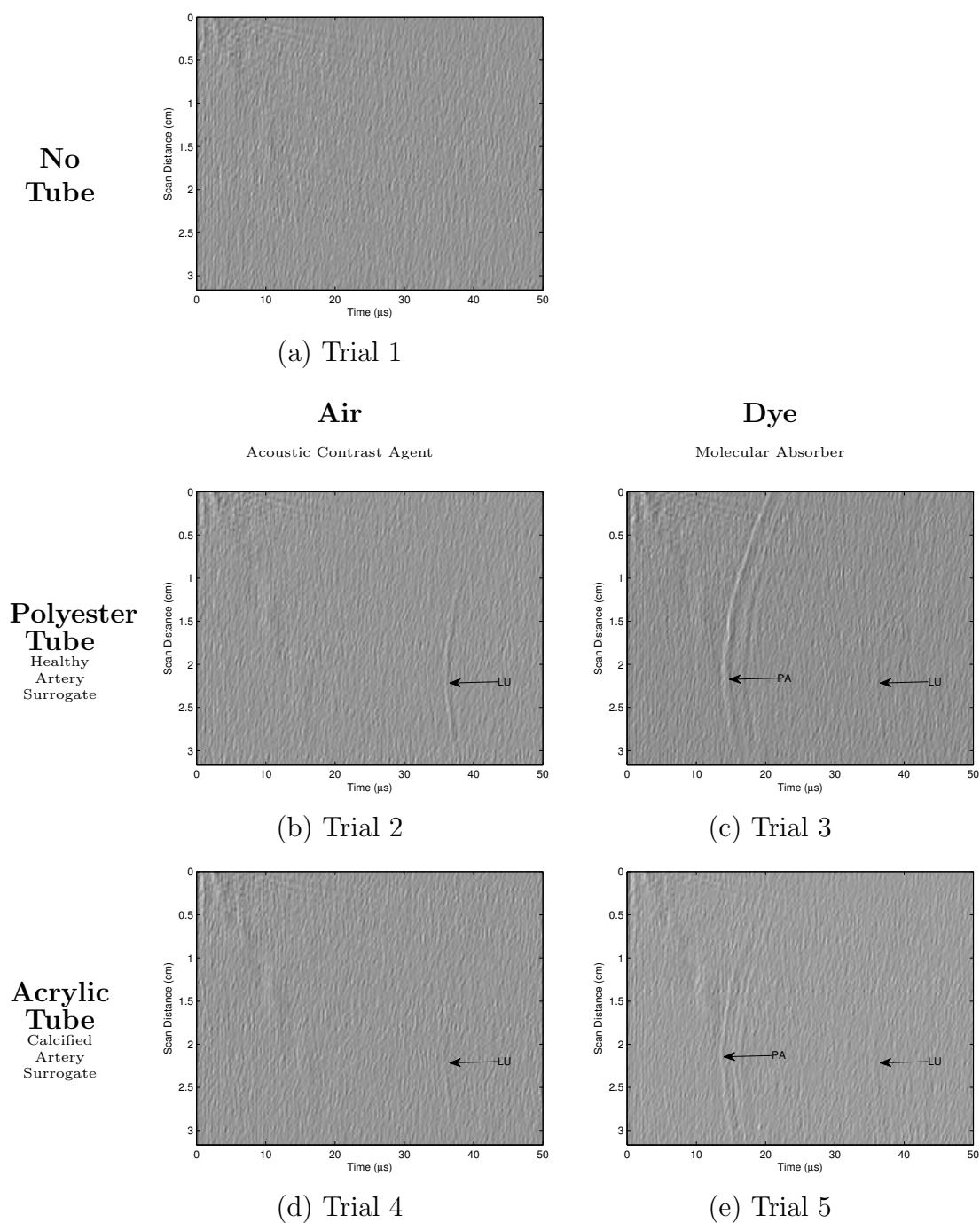
Figure 6.6: F-k filtered B-scan images. The direct wave was successfully suppressed in each trial, allowing for the PA and LU waves in each trial to be more clearly distinguished.
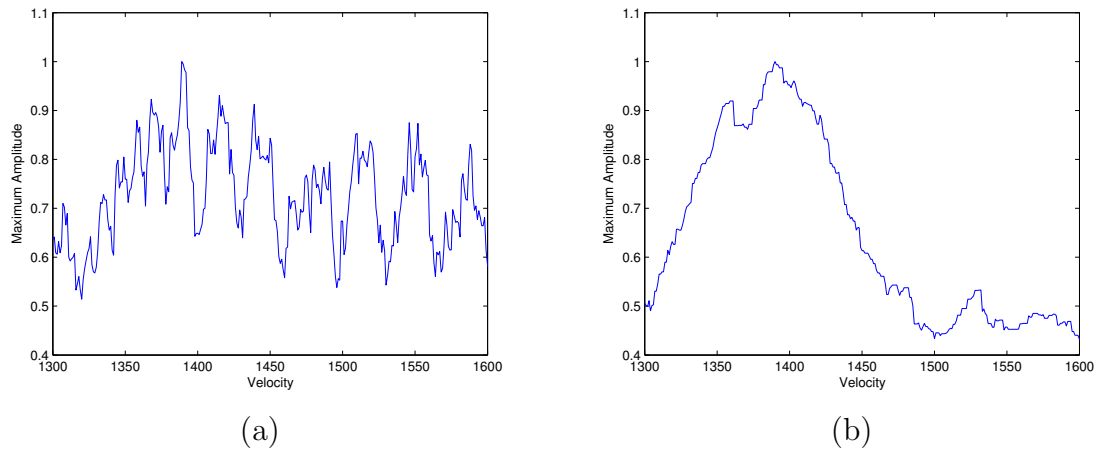
Figure 6.7: Maximum amplitude of LU wave in Trial 2 (a) and PA wave in Trial 3 (b) for a given velocity. The velocity of sound in the phantom for optimum NMO correction was 1390 m/s.

or scatterer (LU). Using the equation for a hyperbola defined in Equation 5.4, and correcting for the increased offset of the source and corresponding travel time for LU waves using Equations 5.5 and 5.6, the arrival of PA and scattered LU waves were placed at the corrected time of arrival. Optimum semblance was found using a speed of sound 1390 m/s for both PA and LU corrections, Figure 6.7.

With the waves arriving at the "correct" times, multiplication of the time axis by velocity resulted in an image in spatial dimensions only, with the tubes located at the appropriate depth, Figure 6.8 and Figure 6.9.

Finally, a stacking procedure was implemented, in which we summed adjacent A-scans into a single trace and normalized. The contrast in relation to each wave, whether generated by the PA effect or LU scattering was comparable through analysis of this trace. The resulting stacked traces after NMO correction assuming PA and LU time of arrival assumptions are shown in Figure 6.10 and 6.11, respectively. Relative contrasts from each trial are displayed in Table 6.1.

**No
Tube**

(a) Trial 1

Air

Acoustic Contrast Agent

Dye

Molecular Absorber

**Polyester
Tube**
Healthy
Artery
Surrogate

(b) Trial 2

(c) Trial 3

**Acrylic
Tube**
Calcified
Artery
Surrogate
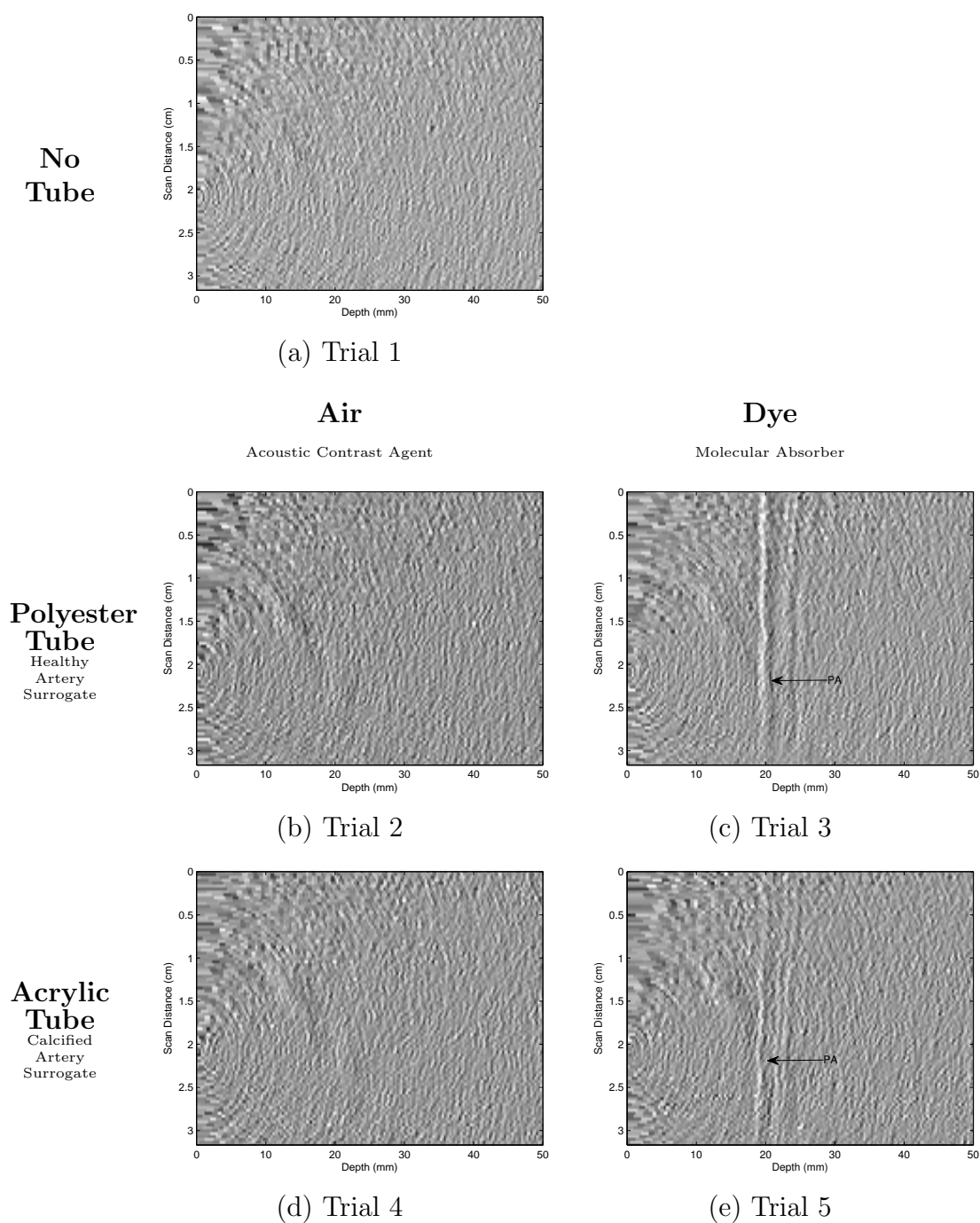
(d) Trial 4

(e) Trial 5

Figure 6.8: NMO corrected images assuming photoacoustic time of arrival geometry.
The PA waves generated in Trial 3 (c) and Trial 5 (e) are located at the correct depth
with hyperbolic arrival due to offset removed.

No Tube

(a) Trial 1

Air

Acoustic Contrast Agent

Dye

Molecular Absorber

Polyester Tube

Healthy Artery Surrogate

(b) Trial 2

(c) Trial 3

Acrylic Tube

Calcified Artery Surrogate
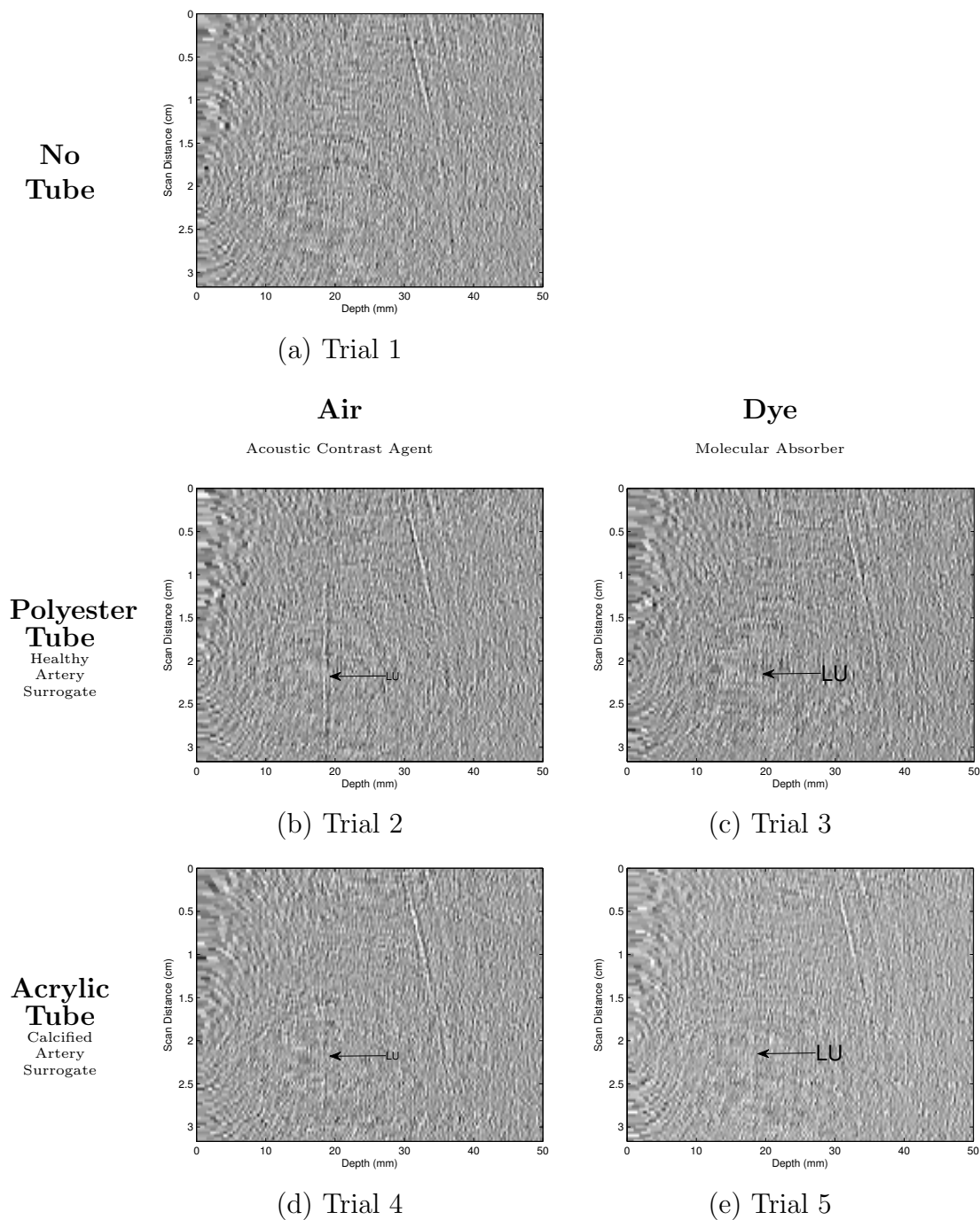
(d) Trial 4

(e) Trial 5

Figure 6.9: NMO corrected images, using laser-ultrasound time of arrival assumptions. Hyperbolic time of arrival behavior was corrected. Trial 2 (b) clearly shows the highest contrast, while Trial 4 (d) and Trial 5 (e) appear to show similar levels of contrast. The scattered LU wave in Trial 3 (c) is not clearly distinguishable.

(a) Trial 1

Air

Acoustic Contrast Agent

Dye

Molecular Absorber

Polyester Tube
Healthy
Artery
Surrogate

Acrylic Tube
Calcified
Artery
Surrogate

(b) Trial 2

(c) Trial 3

(e) Trial 4
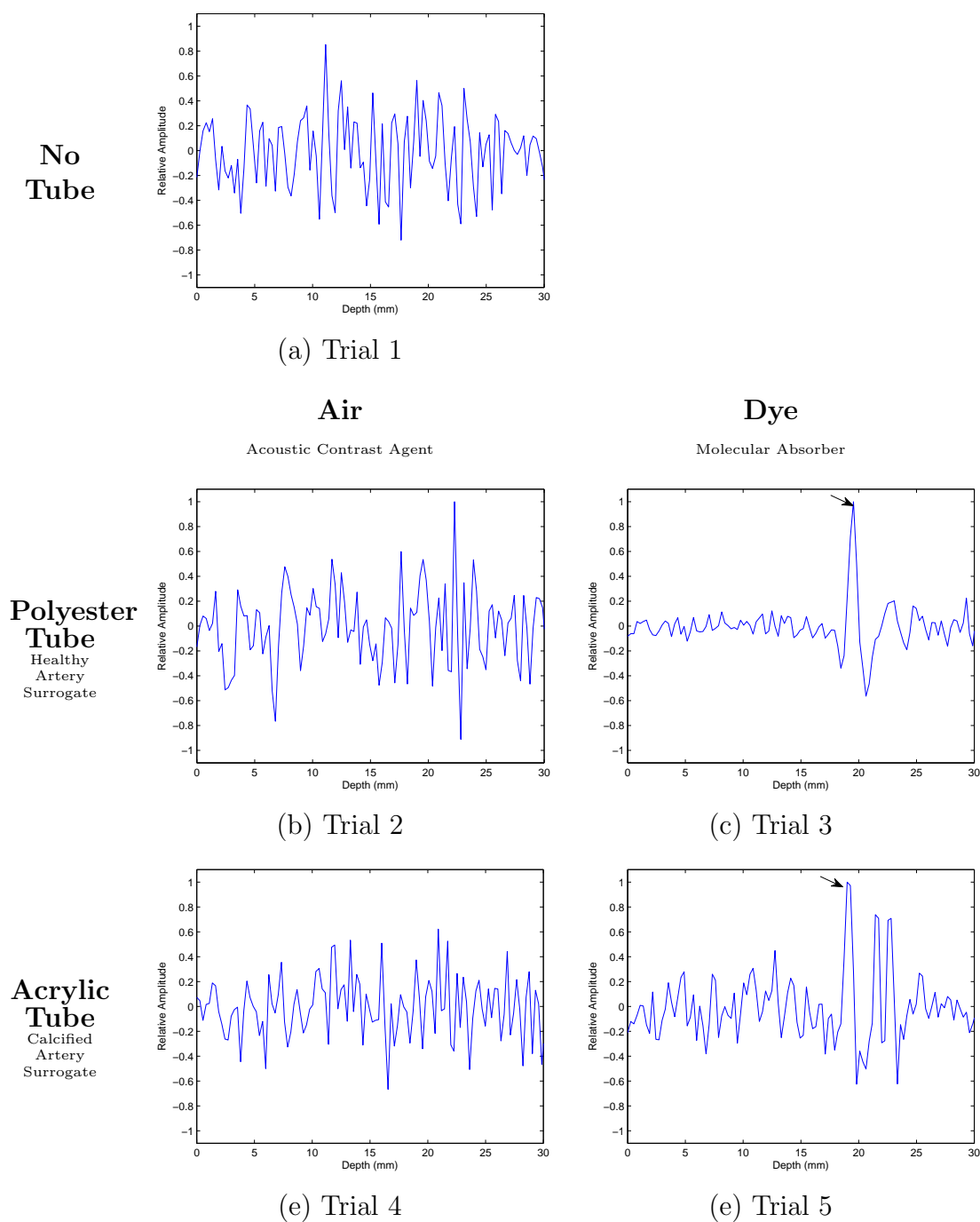
(e) Trial 5

Figure 6.10: Stacked traces after NMO correction using PA time of arrival assumptions. The arrival of PA waves in Trial 3 (c) and Trial 5 (e) are of high contrast, with (c) exhibiting the highest signal-to-noise ratio. Each PA wave arrival is labeled with an arrow.

(a) Trial 1

Air
Acoustic Contrast Agent

Dye
Molecular Absorber

(b) Trial 2

(c) Trial 3

(d) Trial 4

(e) Trial 5
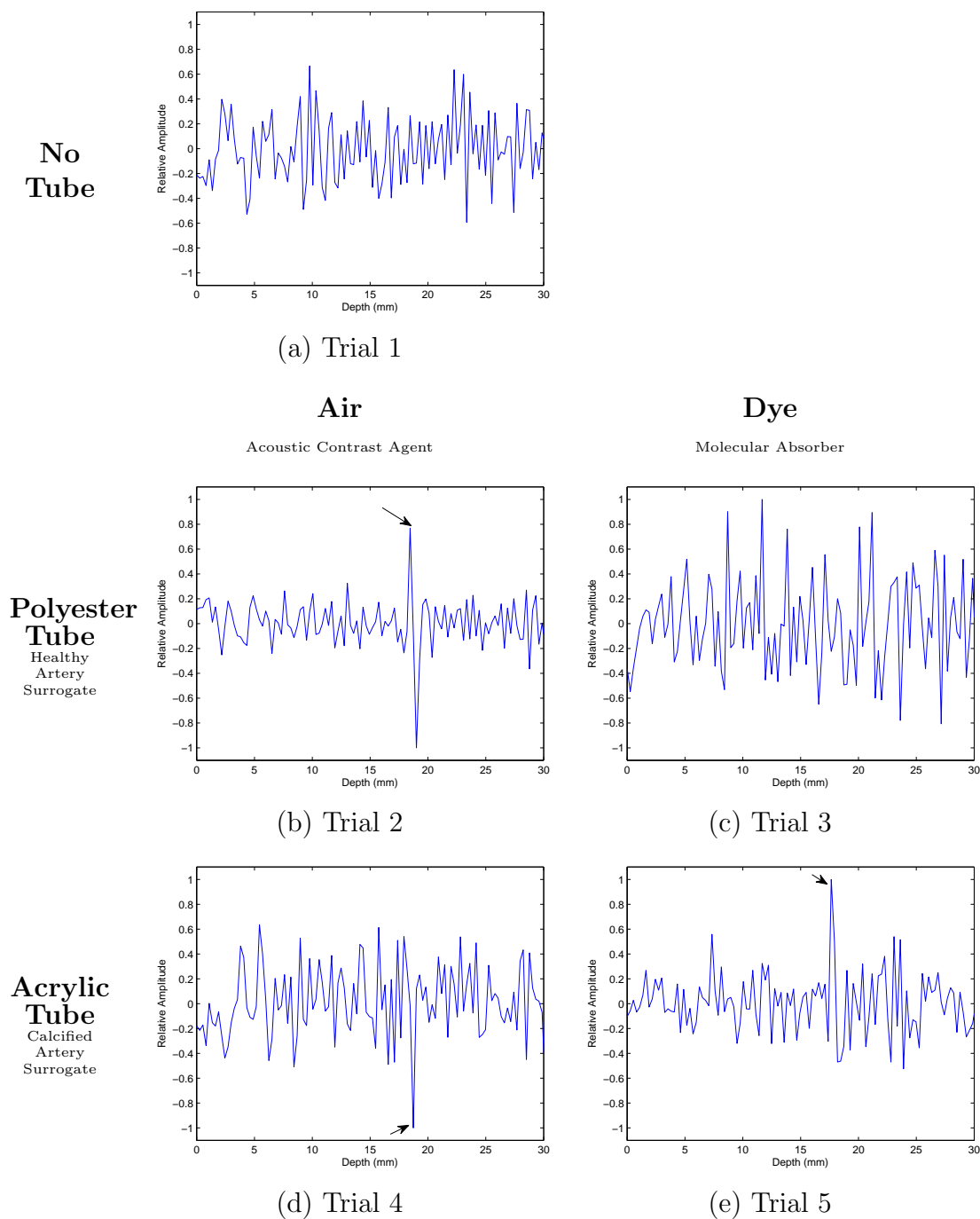
Figure 6.11: Stacked traces from NMO corrected images using LU time of arrival assumptions. Trials 2 (b), 4 (d) and 5 (e) show clearly identifiable arrivals of LU scattered waves, denoted by an arrow. Trial 3 (c), with an acoustically transparent tube filled with dye, does not show a clear LU wave arrival.

	Trial 1	Trial 2	Trial 3	Trial 4	Trial 5
PA Contrast	–	–	8.3	–	2.2
LU Contrast	–	3.1	–	1.7	1.8

Table 6.1: Comparison of contrast for stacked traces after NMO correction with PA and LU time of arrival assumptions for each trial. Large values correspond to a higher ratio of wave amplitude to noise at optimum semblance, and therefore stronger contrast.

6.2.1 Analysis of Photoacoustic Contrast

Photoacoustic waves were generated in Trials 3 and 5, where the absorbing dye, analogous to an absorber such as blood or lipids, is in the tubes. Analyzing the semblance ratio of the stacked traces for these trials, Table 6.1, we can see that the amplitude of the PA wave generated in the polyester tube was significantly higher than the wave generated in the thicker acrylic tube. While a slight hyperechoic effect was expected by generation of the PA wave in a stiff tube, the relative volume of dye in each tube plays a stronger role in PA wave amplitude. The thin wall of the polyester tube corresponded to a larger inner diameter than the acrylic tube, which was a similar size, but had a smaller inner diameter due to a thick wall. This allowed a greater volume of dye to reside within the polyester tube than within the acrylic tube. Increased absorption, and a higher PA wave amplitude in Trial 3 than in Trial 5 resulted. As expected, neither the optically clear tubes, nor air generated a PA wave (Trials 2 and 4).

The ability to differentiate the inner diameter and wall thickness of the tube was beginning to be realized in Trial 5. The PA wave was clearly reflected by the backside of the acrylic inner wall (wave 2 in Figure 6.12 (a)). The difference between waves 1 and 2, therefore, accurately represents the inner diameter of the tube. Wave 3 was a combination of the arrival of waves 3a-3c labeled in Figure 6.12 (b). In this
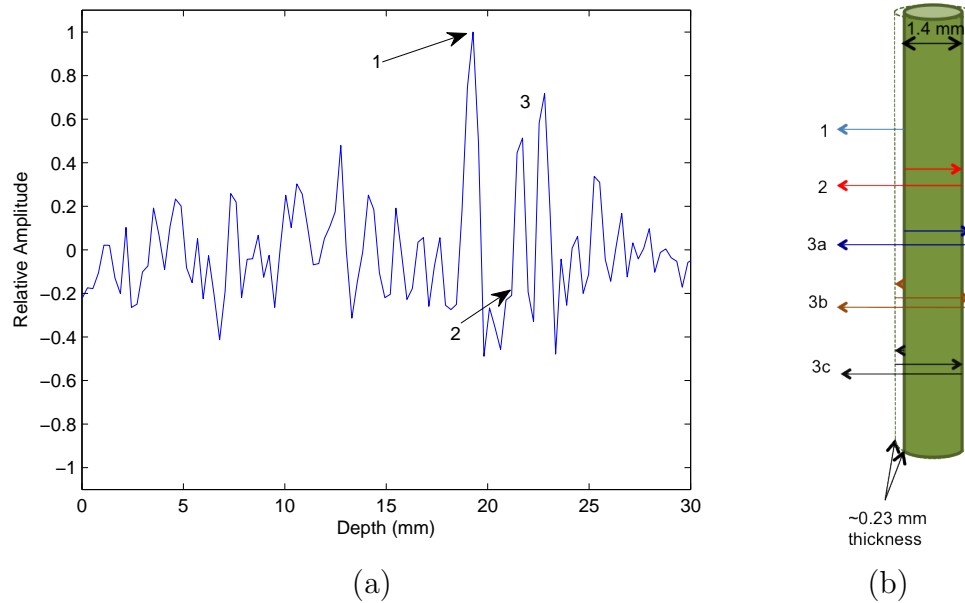
Figure 6.12: (a) Stacked trace from Trial 5, with the acrylic tube filled with dye. Waves arriving from reflections by various phantom- and dye-acrylic interfaces are labeled, corresponding to the wave paths shown in diagram (b). The fine details of the tube wall corresponding to waves 2-3 in (a) are currently unresolved, because reflection paths 2 and 3a-3b in (b) superimposed due to similar time-of-arrivals and a long source wavelength.

experiment, the fine details of reflections by the tube wall were unresolved due to the large wavelength of the LU wave. A similar, but less distinct reflection from the back of the tube was seen in Trial 3, with the polyester tube. By decreasing the wavelength and applying geophysical methods such as amplitude-versus-offset to the unstacked data, we hypothesize that this information can be obtained.

6.2.2   Analysis of Laser-Ultrasound Contrast

Intuitively, it seemed that the acrylic tube should have scattered LU waves stronger than the polyester tube, which is true for the tubes alone. However, the difference between the acoustic impedance of *air* and the phantom was greater than the difference between the acrylic tube and the phantom. The greater volume capacity of the polyester tube allowed more air to reside within the polyester tube than within the thicker-walled acrylic tube. The additional air in Trial 2, therefore, lead to stronger acoustic scattering than Trial 4. This effect is analogous to the increased absorption and PA wave amplitude generated from a greater volume of dye in the polyester tube, discussed in Section 6.2.1.

The acoustic properties of the infrared dye more closely resembled those of the phantom than either air or acrylic (Table 5.1). In addition, the polyester tube was essentially acoustically transparent. As we can see in both Figure 6.9(b) and Figure 6.11(b), any acoustic scattering from the polyester tube filled with dye was indistinguishable. Trials 4 and 5, representative of a calcified artery, exhibited similar levels of contrast due to the strong scattering properties of the acrylic tube. The acrylic tube filled with dye, in fact, exhibited slightly stronger acoustic contrast. While the phantom-acrylic interface was the same in Trials 4 and 5, and in general a direct

interface between the phantom and air (Trial 2) showed higher acoustic contrast than the phantom-dye interface (Trial 3), the addition of the acrylic tube creates a more complicated analysis. Additionally, the NMO corrections derived in Section 5.2.3 are not exact for an unfocused source, therefore small variations in contrast, such as in Trials 4 and 5, should not be considered quantitatively conclusive.

6.2.3 Comparison of PA and LU Resolution and Contrast

The stacked traces clearly show that while the contrast of the PA image was higher than the LU image contrast, the resolution was higher for the LU image. The PA waves had substantially lower frequency content ($\approx$ 500 kHz) than the LU waves ($\approx$ 1 MHz). The theoretical PA frequency, based on the size of the absorbing structure, is in good agreement with this result. The longitudinal dimension of the PA absorber was about 1.5 mm for both tubes, which was the dimension that thermoelastically expanded. This dimension, therefore, corresponded to half of the acoustic wavelength. The theoretical frequency can be approximated $\nu_{PA} = \frac{1390 m/s}{2*1.5mm} \approx 463$ kHz, which is in good agreement with our experimental data. Smaller structures are expected to generate higher frequencies, which we observed with the acrylic tube with a smaller inner diameter (1.4 mm). The wavelength of the LU wave, in contrast, is estimated $\lambda_{LU} = \frac{1390 m/s}{1MHz} \approx 1.4$ mm. We expect structures on the order of 1/4 of the LU wavelength to be resolvable in the LU image ($\approx$ 350 μm).

The signal-to-noise, or contrast, of the PA image was greater than the LU image. This difference was due to the relative absorption strength by water at the surface of the phantom in comparison to absorption by dye in the tube, as well as the strong attenuation of acoustic waves in the phantom. For a 1064 nm source, the absorption

coefficient of our dye ($\approx 20 \text{ cm}^{-1}$) was larger than water ($\approx 0.15 \text{ cm}^{-1}$), which was the primary contributor to absorption in our phantom. The energy of the source beam was significantly attenuated before it reached the dye, yet assuming a factor of 4 of optical energy was attenuated per centimeter (Beard, 2011), the absorption of dye remains substantially larger than absorption by the phantom. Because the amplitude of waves generated by the photoacoustic effect is absorption-based, the PA wave had a higher amplitude. Additionally, the LU wave traveled a longer distance than the PA wave, resulting in greater LU attenuation.

6.2.4 Limitations

- In this experiment, we use a long LU acoustic wavelength, which limits the LU image resolution. This was done in order to provide a large beam for illumination of the dye for PA wave generation. We expect increased resolution for future experiments by reducing the source spot size, and thus reducing the LU wavelength.

- We use a reflective tape to increase detection sensitivity. For this method to be used on patients, a reflective medium would need to be used. Design of a reflective medium that is transparent to the source wavelength, and possibly sterile, could further improve the usability of this method.

- While we were able to detect acoustic impedances analogous to calcification for a thickness of only 233.5 μm, the overall diameter of the tube is greater than 1 mm. Additional experiments are required to confirm the limitations of lateral resolution.

- We report only one image for each trial. For this method of imaging, the PA and LU waves are detected in each of the 95 traces, where each trace is the average of 64 traces. In addition, the stacking procedure implemented provides another form of averaging to ensure the reliability of our results.

CHAPTER 7:

CONCLUSIONS AND FUTURE WORK

7.1 Conclusions

In this work, a method for characterizing vascular structures was presented using remote photoacoustic and laser-ultrasound imaging. Phantom experiments were conducted with absorbers and scatterers embedded. These structures were presented as proxies of healthy vessels and vascular structures corrupted by disease such as atherosclerosis. Using geophysical image processing techniques, we have shown exceptional image resolution and the ability to comparatively analyze PA and LU contrast with an external, noncontact, and nonionizing modality.

We conclude that increased acoustic impedance for a wall thickness less than 250 μm is detectable at depths exceeding 1 cm using external laser-ultrasound. Additionally, the incorporation of an acoustic contrast agent, such as air, greatly improved LU contrast for a thin-walled tube, representative of a healthy vessel, but did not significantly improve contrast for a tube with stronger acoustic contrast, similar to a calcified artery. Moreover, the amplitude of the photoacoustic wave did not significantly increase when generated in a stiff tube in comparison to a thin tube, confirming that differences in acoustic impedance are not readily detected through analysis of photoacoustic wave generation, yet the extent of absorption can be determined from PA waves. The propagation of a PA wave generated in a stiff tube, however, clearly identified the inner diameter of the tube, and showed promise toward distinguishing

the tube wall thickness. Furthermore, contrast relating to both spectroscopic and mechanical properties are comparable using the objective methods described.

7.2   Summary of Contributions

Contributions in this research include:

- developing a method of obtaining both photoacoustic and laser-ultrasound images with a single source and multiple detector positions using noninvasive, nonionizing optical methods;

- joint detection of optical absorbers (analogous to spectroscopically unique molecules in atherosclerotic plaque) and acoustic scatterers (similar to vascular calcifications) at a depth of 18 mm. Structures on the order of 1.5 mm were imaged, with sensitivity to increased acoustic impedance for a wall thickness of only 233.5 μm;

- implementation of geophysical image processing methods to remove interfering direct waves (f-k filter) and remove increased time-of-arrival due to detector offset (normal moveout correction);

- analysis of contrast among absorbers and scatterers through a stacking method commonly used in seismology; and

- showing feasibility of using dual photoacoustic and laser-ultrasound imaging to detect several characteristics of healthy and atherosclerotic vessels, including small amounts of calcifications.

7.3   Future Research

Future research will work toward improved resolution for imaging of smaller structures, particularly scatterers, by reducing the source wavelength. Geophysical techniques, such as amplitude-versus-offset analysis, will be implemented to obtain physical properties and fine details from the image data. Through careful analysis of wave characteristics, we expect to develop the ability to make quantitative conclusions about wall thickness and acoustic impedance of diseased vessels. Further improvements will involve collapsing the waves detected at multiple surface locations to reflect the actual size of the embedded structures.

REFERENCES

Akseli, I., Dey, D., and Cetinkaya, C. 2009. Mechanical Property Characterization of Bilayered Tablets using Nondestructive Air-Coupled Acoustics. *PharmSciTech*, **11**, 90–102.

Allen, T. J., Hall, A., Dhillon, A. P., Owen, J. S., and Beard, P. C. 2012. Spectroscopic photoacoustic imaging of lipid-rich plaques in the human aorta in the 740 to 1400 nm wavelength range. *Journal of Biomedical Optics*, **17**(6), 061209.

Alnaeb, M. E., Alobaid, N., Seifalian, A. M., Mikhailidis, D. P., and Hamilton, G. 2007. Optical Techniques in the Assessment of Peripheral Arterial Disease. *Current Vascular Pharmacology*, **5**(1), 53–59.

Arbab-Zadeh, A., Miller, J. M., Rochitte, C. E., Dewey, M., Niinuma, H., Gottlieb, I., Paul, N., Clouse, M. E., Shapiro, E. P., Hoe, J., Lardo, A. C., Bush, D. E., de Roos, A., Cox, C., Brinker, J., and Lima, J. A. C. 2012. Diagnostic Accuracy of Computed Tomography Coronary Angiography According to Pre-Test Probability of Coronary Artery Disease and Severity of Coronary Arterial Calcification. *Journal of the American College of Cardiology*, **59**(4), 379–387.

Arthurs, Z. M., Bishop, P. D., Feiten, L. E., Eagleton, M. J., Clair, D. G., and Kashyap, V. S. 2010. Evaluation of peripheral atherosclerosis: A comparative analysis of angiography and intravascular ultrasound imaging. *Journal of Vascular Surgery*, **51**(4), 993–939.

Balogun, O., and Murray, T. W. 2011. Frequency domain photoacoustics using

intensity-modulated laser sources. *Nondestructive Testing and Evaluation*, **26**(3-4), 335–351.

Baumgart, D., Schmermund, A., Goerge, G., Haude, M., Ge, J., Adamzik, M., Sehnert, C., Altmaier, K., Groenemeyer, D., Seibel, R., and Erbel, R. 1997. Comparison of Electron Beam Computed Tomography with Intracoronary Ultrasound and Coronary Angiography for Detection of Coronary Atherosclerosis. *Journal of American College of Cardiology*, **30**(1), 57–64.

Beard, J. 2011. Biomedical photoacoustic imaging. *Interface Focus*, **1**, 602–631.

Beard, P. C., Zhang, E. Z., and Laufer, J. G. 2009. *3D Photoacoustic Scanner Based on an Optical Ultrasound-Mapping System for Imaging Superficial Vascular Anatomy* In Vivo. CRC Press.

Bell, A. G. 1880. On the Production and Reproduction of Sound by Light. *American Journal of Sciences*, 305–325.

Bing, W., Guo, T., Hua, W., and Bolei, T. 2011. Extracting near-borehole P and S reflections from array sonic logging data. *Journal of Geophysics and Engineering*, **8**, 308–315.

Bloomfield, P. E., Lo, W. J., and Lewin, P. A. 2000. Experimental Study of the Acoustical Properties of Polymers Utilized to Construct PVDF Ultrasonic Transducers and the Acousto-Electric Properties of PVDF and P(VDF/TrFE) Films. *IEEE Transactions on Ultrasonics, Ferroelectrics, and Frequency Control*, **47**(6), 1397–1404.

Blum, Thomas E., Snieder, Roel, VanWijk, Kasper, and Willis, Mark E. 2011. Theory and laboratory experiments of elastic wave scattering by dry planar fractures. *J. Geophys. Res.*, **116**(aug), B08218.

Briley-Saebo, K. C., Mulder, W. J. M., Mani, V., Hyafil, F., Amirbekian, V., Aguinaldo, J. G. S., Fisher, E. A., and Fayad, Z. A. 2007. Magnetic Resonance Imaging of Vulnerable Atherosclerotic Plaques: Current Imaging Strategies and Molecular Imaging Probes. *Journal of Magnetic Resonance Imaging*, **26**, 460–479.

Burke, A. P., Farb, A., Kolodgie, F. D., Malcom, G. T., and Virmani, R. 1997. Healed ruptured plaques are frequent in men with severe coronary disease and are associated with elevated total/high density lipoprotein (HDL) cholesterol. *Circulation*, **96**(8), Abstract.

Burke, A. P., Taylor, A., Farb, A., Malcom, G. T., and Virmani, R. 2000. Coronary calcification: insights from sudden coronary death victims. *Zeitschrift fr Kardiologie*, **89**, Abstract.

Carp, S. A., Guerra, A., Duque, S. Q., and Venugopalan, V. 2004. Optoacoustic imaging using interferometric measurement of surface displacement. *Applied Physics Letters*, **85**(23), 5772–5774.

Cubeddu, R., Pifferi, A., Taroni, P., Torricelli, A., and Valentini, G. 1997. A solid tissue phantom for photon migration studies. *Physics in Medicine and Biology*, **42**, 1971–1979.

Dale, P. S., Graham, J., Nichols, K. W., Catchings, T., and Richards, M. 2006.

Mammography as a screening tool for peripheral vascular disease. *The American Journal of Surgery*, **192**(4), 488–491.

Driver, I., Feather, J. W., King, P. R., and Dawson, J. B. 1989. The optical properties of aqueous suspensions of Intralipid, a fat emulsion. *Physics in Medicine and Biology*, **34**(12), 1927–1930.

Duck, F. A. 1990. *Physical properties of tissue.* Academic Press.

Dunkin, J. W., and Levin, F. K. 1973. Effect of normal moveout on a seismic pulse. *Society of Exploration Geophysicists*, **38**(4), 635–642.

Ehara, S., Kobayashi, Y., Yoshiyama, M., Shimada, K., Shimada, Y., Fukuda, D., Nakamura, Y., Yamagishi, H., Takeuchi, K., Naruko, T., Haze, K., Becker, A. E., Yoshikawa, J., and Ueda, M. 2004. Spotty Calcification Typifies the Culprit Plaque in Patients With Acute Myocardial Infaction: An Intravascular Ultrasound Study. *Circulation*, **110**, 3424–3429.

Flock, S. T., Jacques, S. L., Wilson, B. C., Star, W. M., and van Gemert, M. J. C. 1992. Optical Properties of Intralipid: A Phantom Medium for Light Propagation Studies. *Lasers in Surgery and Medicine*, **12**, 510–519.

Fok, P.-W. 2012. Growth of necrotic cores in atherosclerotic plaque. *Mathematical Medicine and Biology*, **29**(4), 301–327.

Fowler, K. A. B., Locken, J. A., Duchesne, J. H., and Williamson, M. R. 2002. US for Detecting Renal Calculi with Nonenhanced CT as a Reference Standard. *Radiology*, **222**, 109–113.

Friedrich, G. J., Moes, N. Y., Muhlberger, V. A., Gabl, C., Mikuz, G., Hausmann, D., Fitzgerald, P. J., and Yock, P. G. 1994. Detection of intralesional calcium by intracoronary ultrasound depends on the histologic pattern. *American Heart Journal*, **128**, 435–441.

Gondrie, M. J. A., van der Graaf, Y., Jacobs, P. C., Oen, A. L., and Mali, W. P. T. M. 2010. The association of incidentally detected heart valve calcification with future cardiovascular events. *European Radiology*, **21**(5), 963–973.

Gonzalez, R. C., and Woods, R. E. 2008. *Digital Image Processing*. 3rd edn. Pearson.

Grimm, J. M., Nikolaou, K., Schindler, A., Hettich, R., Heigl, F., Cyran, C. C., Schwarz, F., Klingel, R., Karpinska, A., Yuan, C., Dichgans, M., Reiser, M. F., and Saam, T. 2012. Characteristics of carotid atherosclerotic plaques of chronic lipid apheresis patients as assessed by In Vivo High-Resolution CMR - a comparative analysis. *Journal of Cardiovascular Magnetic Resonance*, **14**(80), 1–8.

Gusev, V. Ė., and Karabutov, A. A. 1993. *Laser Optoacoustics*. American Institute of Physics.

Ha, S., Carson, A., Agarwal, A., Kotov, N. A., and Kim, K. 2011. Detection and monitoring of the multiple inflammatory responses by photoacoustic and molecular imaging using selectively targeted gold nanorods. *Biomedical Optics Express*, **2**(3), 645–657.

Hagenaars, T., Gussenhoven, E. J., van der Linden, E., and Born, N. 2000. Reproducibility of calcified lesion quantification: a longitudinal intravascular ultrasound study. *Ultrasound in Medicine and Biology*, **26**(7), 1075–1079.

Hansson, G. K. 2005. Mechanisms of Disease: Inflammation, Atherosclerosis, and Coronary Artery Disease. *The New England Journal of Medicine*, **352**(16), 1685–1695.

Hayabuchi, Y., Mori, K., Kitagawa, T., Sakata, M., and Kagami, S. 2007. Polytetrafluoroethylene graft calcification in patients with surgically repaired congenital heart disease: Evaluation using multidetector-row computed tomography. *American Heart Journal*, **153**(5), 806.e1–e8.

Hayashi, N., and Sato, M. 2010. F-k Filter Designs to Suppress Direct Waves for Bistatic Ground Penetrating Radar. *IEEE Transactions on Geoscience and Remote Sensing*, **48**(3), 1433–1444.

He, Z. X., Hedrick, T. D., Pratt, C. M., Verani, M. S., Aquino, V., Roberts, R., and Mahmarian, J. J. 2000. Severity of Coronary Artery Calcification by Electron Beam Computed Tomography Predicts Silent Myocardial Ischemia. *Circulation*, **101**, 244–251.

Hecht, E. 2002. *Optics.* 4th edn. Addison Wesley.

Hiratzka, L. F., Eagle, K. A., Liang, L., Fonarow, G. C., LaBresh, K. A., and Peterson, E. D. 2007. Atherosclerosis Secondary Prevention Performance Measures After Coronary Bypass Graft Surgery Compared With Percutaneous Catheter Intervention and Nonintervention Patients in the Get With the Guidelines Database. *Circulation*, **116**, I.

Hochreiner, A., Berer, T., Grün, H., Leitner, M., and Burgholzer, P. 2012. Photoa-

coustic imaging using an adaptive interferometer with a photorefractive crystal. *Journal of Biophotonics*, **5**(7), 508–517.

Hoffmann, U., Ferencik, M., Cury, R. C., and Pena, A. J. 2006. Coronary CT Angiography. *Journal of Nuclear Medicine*, **47**(5), 797–806.

Holmgren, A., Rumsby, G., Gustafsson, S., Nslund, U., and Henein, M. Y. 2012. The nature of cardiac calcification in aortic stenosis. *International Journal of Cardiology*, **158**, 319–321.

Holotta, M., Grossauer, H., Kremser, C., Torbica, P., Völkl, J., Degenhart, G., Esterhammer, R., Nuster, R., Paltauf, G., and Jaschke, W. 2011. Photoacoustic tomography of *ex vivo* mouse hearts with myocardial infarction. *Journal of Biomedical Optics*, **16**(3), 036007.

Jorge-Herrero, E., Fonseca, C., Barge, A. P., Turnay, J., .Olmo, N, Fernández, P., Lizarbe, M. A., and Páez, J. M. García. 2010. Biocompatibility and Calcification of Bovine Pericardium Employed for the Construction of Cardiac Bioprostheses. *Artificial Organs*, **34**(5), E168–E176.

Kang, J., Kim, E., Kwak, J. Y., Yoo, Y., Song, T., and Chang, J. H. 2011. Optimal laser wavelength for photoacoustic imaging of breast microcalcifications. *Applied Physics Letters*, **99**, 153702.

Kihm, H., Carp, S. A., and Venugopalan, V. 2009. *Interferometry-Based Optoacoustic Tomography.* CRC Press.

Kim, C., Erpelding, T. N., Jankovic, L., Pashley, M. D., and Wang, L. V. 2010.

Deeply penetrating in vivo photoacoustic imaging using a clinical ultrasound array system. *Biomedical Optics Express*, **1**(1), 278–284.

Kim, C., Erpelding, T. N., Jankovic, L., and Wang, L. V. 2011. Performance benchmarks of an array-based hand-held photoacoustic probe adapted from a clinical ultrasound system for non-invasive sentinel lymph node imaging. *Philosophical Transactions of The Royal Society*, **369**, 4644–4650.

Kim, K., Huang, S. W., Ashkenazi, S., O'Donnell, M., Agarwal, A., Kotov, N. A., Denny, M. F., and Kaplan, M. J. 2007. Photoacoustic imaging of early inflammatory response using gold nanorods. *Applied Physics Letters*, **90**(22), 223901.

Kinnunen, M., and Myllylä, R. 2005. Effect of glucose on photoacoustic signals at the wavelengths of 1064 nm and 532 nm in pig blood and intralipid. *Journal of Physics D: Applied Physics*, **38**, 2654–2661.

Kolkman, R. G. M., Blomme, E., Cool, T., Bilcke, M., van Leeuwen, T. G., Steenbergen, W., Grimbergen, K. A., and den Heeten, G. J. 2010. Feasibility of noncontact piezoelectric detection of photoacoustic signals in tissue-mimicking phantoms. *Journal of Biomedical Optics*, **15**(5), 055011.

Kolodgie, F. D., Burke, A. P., Farb, A., Gold, H. K., Yuan, J., Narula, J., Finn, A. V., and Virmani, R. 2001. The thin-cap fibroatheroma: a type of vulnerable plaque: the major precursor lesion to acute coronary syndromes. *Current Opinion in Cardiology*, **16**(5), 285–292.

Lattermann, A., Matthäus, C., Bergner, N., Beleites, C., Romeike, B. F., Krafft,

C., Brehm, B. R., and Popp, J. 2013. Characterization of atherosclerotic plaque depositions by Raman and FTIR imaging. *Journal of Biophotonics*, **6**(1), 110–121.

Laufer, J., Zhang, E., and Beard, P. 2010. Evaluation of Absorbing Chromophores Used in Tissue Phantoms for Quantitative Photoacoustic Spectroscopy and Imaging. *IEEE Journal of Selected Topics in Quantum Electronics*, **16**(3), 600–607.

Li, C., Li, S., Guan, G., Wei, C., Huang, Z., and Wang, R. K. 2012a. A comparison of laser ultrasound measurements and finite element simulations for evaluating the elastic properties of tissue mimicking phantoms. *Optics and Laser Technology*, **44**, 866–871.

Li, M., and Hayward, G. 2012. Ultrasound Nondestructive Evaluation (NDE) Imaging with Transducer Arrays and Adaptive Processing. *Sensors*, **12**, 42–54.

Li, X., Wei, W., Zhou, Q., Shung, K. K., and Chen, Z. 2012b. Intravascular photoacoustic imaging at 35 to 80 MHz. *Journal of Biomedical Optics*, **17**(10), 106005.

Mars, J., III, J. W. Rector, and Lazaratos, S. K. 1997. Filter formulation and wavefield separation of cross-well seismic data. *Geophysical Prospecting*, **47**, 611–636.

Mendis, S., Puska, P., and Norrving, B. (eds). 2011. *Global Atlas on cardiovascular disease prevention and control*. WHO.

Moussa, I., Mario, C. D., Moses, J., Reimers, B., Francesco, L. D., Martini, G., Tobis, J., and Colombo, A. 1997. Coronary Stenting after Rotational Atherectomy in Calcified and Complex Lesions: Angiographic and Clinical Follow-Up Results. *Circulation*, **96**(1), 128–136.

Naghavi, M., Libby, P., Falk, E., Casscells, S. W., Litovsky, S., Rumberger, J., Badimon, J. J., Stefanadis, C., Moreno, P., Pasterkamp, G., Fayad, Z., Stone, P. H., Waxman, S., Raggi, P., Madjid, M., Zarrabi, A., Burke, A., Yuan, C., Fitzgerald, P. J., Siscovick, D. S., Korte, C. L. De, Aikawa, M., Airaksinen, K. E. J., Assmann, G., Becker, C. R., Chesebro, J. H., Farb, A., Galis, Z. S., Jackson, C., Jang, I. K., Koenig, W., Lodder, R. A., March, K., Demirovic, J., Navab, M., Priori, S. G., Rekhter, M. D., Bahr, R., Grundy, S. M., Mehran, R., Colombo, A., Boerwinkle, E., Ballantyne, C., W. Insull, Jr., Schwartz, R. S., Vogel, R., Serruys, P. W., Hansson, G. K., Faxon, D. P., Kaul, S., Drexler, H., Greenland, P., Muller, J. E., Virmani, R., Ridker, Pl. M., Zipes, D. P., Shah, P. K., and Willerson, J. T. 2003. From Vulnerable Plaque to Vulnerable Patient: A Call for New Definitions and Risk Assessment Strategies: Part I. *Circulation*, **108**, 1664–1672.

Nicholls, S. J., Tuzcu, M., Wolski, K., Sipahi, I., Schoenhagen, P., Crowe, T., Kapadia, S. R., Hazen, S. L., and Nissen, S. E. 2007. Coronary Artery Calcification and Changes in Atheroma Burden in Response to Established Medical Therapies. *Journal of the American College of Cardiology*, **49**(2), 263–270.

Niederhauser, J. J., Jaeger, M., Hejazi, M., Keppner, H., and Frenz, M. 2007. Transparent ITO coated PVDF transducer for optoacoustic depth profiling. *Optics Communications*, **253**, 401–406.

Nuster, R., Gratt, S., Passler, K., Meyer, D., and Paltauf, G. 2012. Photoacoustic section imaging using an elliptical acoustic mirror and optical detection. *Journal of Biomedical Optics*, **17**(3), 030503.

O'Rourke, R. A., Brundage, B. H., Froelicher, V. F., Greenland, P., Grundy, S. M.,

Hachamovitch, R., Pohost, G. M., Shaw, L. J., Weintraub, W. S., W. L. Winters, Jr., Forrester, J. S., Douglas, P. S., Faxon, D. P., Fisher, J. D., Gregoratos, G., Hochman, J. S., A. M. Hutter, Jr., Kaul, S., Weintraub, W. S., W. L. Winters, Jr., and Wolk, M. J. 2000. American College of Cardiology/American Heart Association Expert Consensus Document on Electron-Beam Computed Tomography for the Diagnosis and Prognosis of Coronary Artery Disease. *Circulation*, **102**(1), 126–140.

Paltauf, G., Nuster, R., Haltmeier, M., and Burgholzer, P. 2007a. Experimental evaluation of reconstruction algorithms for limited view photoacoustic tomography with line detectors. *Inverse Problems*, **23**, S81–S94.

Paltauf, G., Nuster, R., Haltmeier, M., and Burgholzer, P. 2007b. Photoacoustic tomography using a Mach-Zehnder interferometer as an acoustic line detector. *Applied Optics*, **46**(16), 3352–3358.

Pasterkamp, G., Schoneveld, A. H., van der Wal, A. C., Hijnen, D.-J., van Wolveren, W. J. A., Plomp, S., Teepen, H. L. J. M., and Borst, C. 1999. Inflammation of the Atherosclerotic Cap and Shoulder of the Plaque is a Common and Locally Observed Feature in Unruptured Plaques of Femoral and Coronary Arteries. *Arteriosclerosis, Thrombosis, and Vascular Biology*, **19**(1), 54–59.

Pavan, T. Z., Madsen, E. L., Frank, G. R., Corneiro, A. A. O., and Hall, T. J. 2010. Nonlinear elastic behavior of phantom materials for elastography. *Physics in Medicine and Biology*, **55**, 2679–2962.

Payne, B. P., Venugopalan, V., Mimić, B. B., and Nishioka, N. S. 2003. Optoacoustic

tomography using time-resolved interferometric detection of surface displacement. *Journal of Biomedical Optics*, **8**(2), 273–280.

Pouet, B., Wartelle, A., and Breugnot, S. 2011. Multi-detector receiver for laser ultrasonic measurement on the run. *Nondestructive Testing and Evaluation*, **26**(3-4), 253–266.

Raggi, P., and Bellasi, A. 2007. Clinical Assessment of Vascular Calcification. *Advances in Chronic Kidney Disease*, **14**(1), 37–43.

Raggi, P., Bellasi, A., Gamboa, C., Ferramosca, E., Ratti, C., Block, G. A., and Muntner, P. 2011. All-cause Mortality in Hemodialysis Patients with Heart Valve Calcification. *Clinical Journal American Society of Nephrology*, **6**, 1990–1995.

Rhoades, R., and Pflanzer, R. (eds). 2003. *Human Physiologyl.* Thomson Learning.

Richards-Kortum, R. 2010. *Biomedical Engineering for Global Health.* Cambridge.

Richardson, P. D., Davies, M. J., and Born, G. V. R. 1989. Influence of plaque configuration and stress distribution on fissuring of coronary atherosclerotic plaques. *The Lancet*, **334**, 941–994.

Roger, V. L., Go, A. S., Lloyd-Jones, D. M., Adams, R. J., Berry, J. D., Brown, T. M., Carnethon, M. R., Dai, S., de Simone, G., Ford, E. S., Fox, C. S., Fullerton, H. J., Gillespie, C., Greenlund, K. J., Hailpern, S. M., Heit, J. A., Ho, P. M., Howard, V. J., Kissela, B. M., Kittner, S. J., Lackland, D. T., Lichtman, J. H., Lisabeth, L. D., Makuc, D. M., Marcus, G. M., Marelli, A., Matchar, D. B., Mc-Dermott, M. M., Meigs, J. B., Moy, C. S., Mozaffarian, D., Mussolino, M. E., Nichol, G., Paynter, N. P., Rosamond, W. D., Sorlie, P. D., Stafford, R. S., Turan,

T. N., Turner, M. B., Wong, N. D., and Wylie-Rosett, J. 2011. Heart Disease and Stroke Statistics–2011 Update: A Report From the American Heart Association. *Circulation*, **123**, e18–e209.

Rupert, G. B., and Chun, J. H. 1975. The block move sum normal moveout correction. *Geophysics*, **40**(1), 17–24.

Saam, T., Hatsukami, T. S., Takaya, N., Chu, B., Underhill, H., Kerwin, W. S., Cai, J., Ferguson, M. S., and Yuan, C. 2007. Noninvasive MR Imaging for Characterization and Assessment. *Radiology*, **244**(1), 64–77.

Sangiorgi, G., Rumberger, J. A., Severson, A., Edwards, W. D., Gregoire, J., Fitzpatrick, L. A., and Schwartz, R. S. 1998. Arterial Calcification and Not Lumen Stenosis Is Highly Correlated With Atherosclerotic Plaque Burden in Humans: A Histologica Study of 723 Coronary Artery Segments Using Nondecalcifying Methodology. *Journal of the American College of Cardiology*, **31**(1), 126–133.

Schuijf, J. D., Beck, T., Burgstahler, C., Jukema, J. Wouter, Dirksen, M. S., Roos, A. De, der Wall, E. E. Van, Schroeder, S., Wijns, W., and Bax, J. J. 2007. Differences in plaque composition and distribution in stable coronary artery disease versus acute coronary syndromes; non-invasive evaluation with multi-slice computed tomography. *Acute Cardiac Care*, **9**, 48–53.

Selfridge, A. R. 1985. Approximate Material Properties in Isotropic Materials. *IEEE Transactions on Sonics and Ultrasonics*, **SU-32**(3), 381–394.

Sethuraman, S., Aglyamov, S., Amirian, J., Smalling, R., and Emelianov, S. 2005.

Intravascular Photoacoustic Imaging to Detect and Differentiate Atherosclerotic Plaques. *IEEE Ultrasonics Symposium*, **1**, 133–136.

Taki, H., Sakamoto, T., Yamakawa, M., Shiina, T., and Sato, T. 2012. Small calcification indicator in ultrasonography using correlation of echoes with a modified Wiener filter. *J Med Ultrasonics*, **39**, 127–135.

Thomas, D. B., Whitehead, J., Dorse, C., Threatt, B. A., F. I. Gilbert, Jr., Present, A. J., and Carlile, T. 1993. Mammographic Calcifications and Risk of Subsequent Breast Cancer. *Journal of the National Cancer Institute*, **85**, 230–235.

Thomas, D. B., Carter, R. A., W. H. Bush, Jr., Ray, R. M., Stanford, J. L., Lehman, C. D., Daling, J. R., Malone, K., and Davis, S. 2002. Risk of Subsequent Breast Cancer in Relation to Characteristics of Screening Mammograms from Women Less Than 50 Years of Age. *Cancer Epidemiology Biomarkers and Prevention*, **11**, 565–571.

Verghese, I., and Cetinkaya, C. 2007. Noncontact Photo-Acoustic Defect Detection in Drug Tablets. *Journal of Pharmaceutical Sciences*, **96**(8), 2125–2133.

Virmani, R., Kolodgie, F. D., Burke, A. P., Farb, A., and Schwartz, S. M. 2000. From Sudden Coronary Death: A Comprehensive Morphological Classification Scheme for Atherosclerotic Lesionsl. *Arteriosclerosis, Thrombosis, and Vascular Biology*, **20**(5), 1262–1275.

Wang, B., Karpiouk, A., Yeager, D., Amirian, J., Litovsky, S., Smalling, R., and Emelianov, S. 2012. *In vivo* intravascular ultrasound-guided photoacoustic imaging

of lipid in plaques using an animal model of atherosclerosis. *Ultrasound in Medicine and Biology*, **38**(12), 2098–2103.

Wang, L.V. (ed). 2009. *Photoacoustic Imaging and Spectroscopy.* CRC Press.

Wang, Y., Li, C., and Wang, R. K. 2011. Noncontact photoacoustic imaging achieved by using a low-coherence interferometer as the acoustic detector. *Optics Letters*, **36**(20), 3975–3977.

Wang, Z., Kyono, H., Bezerra, H. G., Wang, H., Gargesha, M., Alraies, C., Xu, C., Schmitt, J. M., Wilson, D. L., Costa, M. A., and Rollins, A. M. 2010. Semiautomatic segmentation and quantification of calcified plaques in intracoronary optical coherence tomography images. *Journal of Biomedical Optics*, **16**(6), 061711.

Webster, J. G. (ed). 1998. *Medical Instrumentation: Application and Design.* Wiley.

Wexler, L., Brundage, B., Crouse, J., Detrano, R., Fuster, V., Maddahi, J., Rumberger, J., Stanford, W., White, R., and Taubert, K. 1996. Coronary Artery Calcification: Pathophysiology, Epidemiology, Imaging Methods, and Clinical Implications. *Circulation*, **94**(5), 1175–1192.

Xu, M., and Wang, L. 2006. Photoacoustic imaging in biomedicine. *Review of Scientific Instruments*, **77**, 041101.

Yao, J., and Wang, L. V. 2011. Photoacoustic tomography: fundamental advances and prospects. *Contrast Media and Molecular Imaging*, **6**(5), 332–345.

Yao, L., Sun, Y., and Jiang, H. 2010. Transport-based quantitative photoacoustic tomography: simulations and experiments. *Physics in Medicine and Biology*, **55**, 1917–1934.

Yeager, D., Karpiouk, A., Wang, B., Amirian, J., Sokolov, K., Smalling, R., and Emelianov, S. 2012. Intravascular photoacoustic imaging of exogenously labeled atherosclerotic plaque through luminal blood. *Journal of Biomedical Optics*, **17**(10), 106016.

Yokoyama, N., Konno, K., Suzuki, S., and Isshiki, T. 2007. Serial Assessment of Liquefaction Necrosis of Mitral Annular Calcification by Echocardiography and Multislice Computed Tomography. *Circulation*, **115**, e1–e2.

Zhang, E., Laufer, J., and Beard, P. 2008. Backward-mode multiwavelength photoacoustic scanner using a planar Fabry-Perot polymer film ultrasound sensor for high-resolution three-dimensional imaging of biological tissues. *Applied Optics*, **47**(4), 561–577.

Zhang, E. Z., Povazay, B., Laufer, J., Alex, A., Hofer, B., Pedley, B., Glittenberg, C., Treeby, B., Cox, B., Beard, P., and Drexler, W. 2011. Multimodal photoacoustic and optical coherence tomography scanner using an all optical detection scheme for 3D morphological skin imaging. *Biomedical Optics Express*, **2**(8), 2202–2215.